The Astronomical Journal, 169:30 (25pp), 2025 January https://doi.org/10.3847/1538-3881/ad9265

VLTI/GRAVITY Observations of AF Lep b: Preference for Circular Orbits, Cloudy Atmospheres, and a Moderately Enhanced Metallicity

William O. Balmer[1,2,21], Kyle Franson[3,22], Antoine Chomez[4,5], Laurent Pueyo[2], Tomas Stolker[6], Sylvestre Lacour[4], Mathias Nowak[7,8], Evert Nasedkin[9,10], Markus J. Bonse[11,12], Daniel Thorngren[1], Paulina Palma-Bifani[4,13], Paul Mollière[9], Jason J. Wang[14], Zhoujian Zhang[15,23], Amanda Chavez[14], Jens Kammerer[16], Sarah Blunt[14,15], Brendan P. Bowler[3], Mickael Bonnefoy[5], Wolfgang Brandner[9], Benjamin Charnay[4], Gael Chauvin[13], Th. Henning[9], A.-M. Lagrange[4,5], Nicolas Pourré[5], Emily Rickman[17], Robert De Rosa[18], Arthur Vigan[19], and Thomas Winterhalder[20]
[1] Department of Physics & Astronomy, Johns Hopkins University, 3400 N. Charles Street, Baltimore, MD 21218, USA; wbalmer1@jhu.edu
[2] Space Telescope Science Institute, 3700 San Martin Drive, Baltimore, MD 21218, USA
[3] Department of Astronomy, The University of Texas at Austin, Austin, TX 78712, USA
[4] LESIA, Observatoire de Paris, PSL, CNRS, Sorbonne Université, Université de Paris, 5 place Janssen, 92195 Meudon, France
[5] Univ. Grenoble Alpes, CNRS, IPAG, 38000 Grenoble, France
[6] Leiden Observatory, Leiden University, Einsteinweg 55, 2333 CC Leiden, The Netherlands
[7] Institute of Astronomy, University of Cambridge, Madingley Road, Cambridge CB3 0HA, 939, UK
[8] Kavli Institute for Cosmology, University of Cambridge, Madingley Road, Cambridge CB3 0HA, UK
[9] Max Planck Institute for Astronomy, Königstuhl 17, 69117 Heidelberg, Germany
[10] School of Physics, Trinity College Dublin, The University of Dublin, Dublin 2, Ireland
[11] ETH Zurich, Institute for Particle Physics & Astrophysics, Wolfgang-Pauli-Str. 27, 8093 Zurich, Switzerland
[12] Max Planck Institute for Intelligent Systems, Max-Planck-Ring 4, 72076 Tubingen, Germany
[13] Laboratoire Lagrange, UniversiteCote d'Azur, CNRS, Observatoire de la Cote d'Azur, 06304 Nice, France
[14] Center for Interdisciplinary Exploration and Research in Astrophysics (CIERA) and Department of Physics and Astronomy, Northwestern University, Evanston, IL 60208, USA
[15] Department of Astronomy & Astrophysics, University of California, Santa Cruz, CA 95064, USA
[16] European Southern Observatory, Karl-Schwarzschild-Str. 2, 85748 Garching, Germany
[17] European Space Agency (ESA), ESA Office, Space Telescope Science Institute, USA
[18] European Southern Observatory, Alonso de Cofdova 3107, Vitacura, Santiago, Chile
[19] Aix Marseille Univ, CNRS, CNES, LAM, Marseille, France
[20] European Southern Observatory, Karl-Schwarzschild-Straße 2, 85748 Garching, Germany
Received 2024 August 30; revised 2024 November 7; accepted 2024 November 8; published 2024 December 16

Abstract

Direct imaging observations are biased toward wide-separation, massive companions that have degenerate formation histories. Although the majority of exoplanets are expected to form via core accretion, most directly imaged exoplanets have not been convincingly demonstrated to follow this formation pathway. We obtained new interferometric observations of the directly imaged giant planet AF Lep b with the VLTI/GRAVITY instrument. We present three epochs of ∼50 μas relative astrometry and the K-band spectrum of the planet for the first time at a resolution of $R = 500$. Using only these measurements, spanning less than 2 months, and the Hipparcos-Gaia Catalogue of Accelerations, we are able to significantly constrain the planet's orbit; this bodes well for interferometric observations of planets discovered by Gaia DR4. Including all available measurements of the planet, we infer an effectively circular orbit ($e < 0.02$, 0.07, and 0.13 at 1σ, 2σ, and 3σ, respectively) in spin–orbit alignment with the host and measure a dynamical mass of $M_p = 3.75 M_{\rm Jup} \pm 0.5 M_{\rm Jup}$. Models of the spectrum of the planet show that it is metal-rich ($[{\rm M/H}] = 0.75 \pm 0.25$), with a C/O abundance encompassing the solar value. This ensemble of results shows that the planet is consistent with core accretion formation.

Unified Astronomy Thesaurus concepts: Optical interferometry (1168); Direct imaging (387); Exoplanet atmospheres (487); Orbit determination (1175); Extrasolar gaseous giant planets (509)

Materials only available in the online version of record: data behind figure

1. Introduction

1.1. Tracing the Formation of Gas Giants with Direct Observations

Gas giants play a central role in shaping the formation and evolution of planetary systems in general and our own solar system in particular (e.g., H. F. Levison & C. Agnor 2003; S. N. Raymond et al. 2014; A. C. Childs et al. 2019; J. Horner et al. 2020a). Once they have formed, giant planets dominate the subsequent production and dynamical evolution of dust, planetesimals, and inner terrestrial planets, likely dictating the volatile content of terrestrial planets (e.g., S. N. Raymond 2008; S. N. Raymond et al. 2012; S. N. Raymond & A. Izidoro 2017; S. Sotiriadis et al. 2018; B. Bitsch et al. 2020; J. Horner et al. 2020b). It has even been suggested recently that the presence of outer giant planets is correlated with inner terrestrial planets (L. J. Rosenthal et al. 2022). As such, it is important to understand the formation and evolution of gas giants in order to better understand the occurrence of Earth-like planets and the emergence of life in the universe. Gas giants

[21] Johns Hopkins University George Owen Fellow.
[22] NSF Graduate Research Fellow.
[23] NASA Sagan Fellow.

themselves are rich laboratories: they host complex moon systems (D. Morrison 1982), bear dramatic storm systems and weather patterns (P. S. Marcus 1993), are obscured by clouds of varying species (C. Helling 2019), and have interiors with poorly constrained structure and composition whose investigation drives advancement in physics modeling and experimentation (W. B. Hubbard et al. 2002; T. Guillot 2005).

High-contrast imaging observations enabled by adaptive optics and coronagraphic instruments have resulted in the discovery of a growing number of directly imaged planets ($M < 13 M_{\rm Jup}$) in wide orbits ($a > 10$ au) around young (<100 Myr) pre-main-sequence stars (for a review, see T. Currie et al. 2023). These objects appear much rarer than shorter-separation gas giants (e.g., E. L. Nielsen et al. 2019; A. Vigan et al. 2021, and references therein), and their formation histories are often debated.

Demographic studies from the larger sample of older radial velocity (RVs) gas giants have shown that (1) the fraction of giant planets orbiting a star increases with stellar metallicity, tracing core accretion, as more solids are found in the planet-forming disks of higher-metallicity stars (G. Gonzalez 1997; N. C. Santos et al. 2004; D. A. Fischer & J. Valenti 2005; C. Mordasini et al. 2012); and (2) planets with masses below about $4 M_{\rm Jup}$ are found orbiting metal-rich host stars, whereas objects with masses above $4 M_{\rm Jup}$ exhibit a much broader range of host star metallicity (N. C. Santos et al. 2017; K. C. Schlaufman 2018). The bulk of gas giants appear to orbit near their host star's ice lines, ∼3–10 au around solar-type stars (R. B. Fernandes et al. 2019; R. A. Wittenmyer et al. 2020; B. J. Fulton et al. 2021; A. M. Lagrange et al. 2023), albeit with a large scatter ranging from ultrahot Jupiters to planets with periods $\gtrsim$1000 yr. Bulk density measurements from transiting planets with RV masses have elucidated a planetary mass versus planetary metallicity trend (T. Guillot et al. 2006; N. Miller & J. J. Fortney 2011; D. P. Thorngren et al. 2016) that is explainable by core accretion (e.g., Y. Hasegawa et al. 2018). At higher masses, planets are generally less metal-rich because they have accreted a larger fraction of H/He gas (D. Thorngren & J. J. Fortney 2019), though these samples are based on short-period planets that are much closer to their stars than directly detected objects. Despite remaining open questions, core accretion formation is the predominant theory of planet formation for the sample of indirectly detected planets (e.g., S. N. Raymond & A. Morbidelli 2022).

Many objects in the current sample of directly imaged exoplanets are broadly consistent with formation in (1) the low-probability, high-mass tail of core accretion model distributions, as well as subsequent dynamical scattering outward (e.g., C. Mordasini et al. 2009; G.-D. Marleau et al. 2019; A. Emsenhuber et al. 2021a, 2021b); (2) the low-probability, low-mass tail of molecular core fragmentation and early dynamical capture distributions (e.g., G. Chabrier 2003; P. Padoan & Å. Nordlund 2004; D. F. A. Boyd & A. P. Whitworth 2005; M. R. Bate 2009, 2012); or perhaps (3) instances of disk instability and fragmentation (e.g., A. P. Boss 1997; K. M. Kratter et al. 2010; D. H. Forgan et al. 2018). There is growing consensus from dynamical studies tracing the eccentricity and obliquity distributions of these systems that directly imaged planets interior to ∼50–100 au formed within a disk (e.g., B. P. Bowler et al. 2020, 2023; A. G. Sepulveda et al. 2024), but it is still unclear whether these objects formed via core accretion or disk fragmentation.

The challenge for direct imaging is twofold: to push to observe planets that are representative of the bulk of the exoplanet population, and to disentangle the formation histories of known imaged planets. Direct observations, combined with model independent mass measurements, can then seek to expand on the observational trends to inform planet formation models with greater fidelity.

1.2. Accessing Solar System Scales with Interferometry

In addition to classical direct imaging using coronagraphic imaging, or molecular mapping via high-resolution cross correlation, optical interferometry has begun to provide direct observations of gas giant planets with the advent of the Very Large Telescope Interferometer (VLTI) GRAVITY instrument (GRAVITY Collaboration et al. 2017) and the ExoGRAVITY survey (S. Lacour et al. 2020). GRAVITY is a fiber-fed instrument with dedicated fringe tracking. Informed by RV observations and proper-motion anomalies (A. Grandjean et al. 2019; A. M. Lagrange et al. 2020), GRAVITY has helped validate and reveal two newly directly detected planets within 10 au, β Pictoris c (2.7 au; M. Nowak et al. 2020) and HD 206893 c (3.5 au; S. Hinkley et al. 2023). With absolute astrometry from Gaia, GRAVITY has detected a handful of brown dwarf companions at very close separations (60–200 mas; N. Pourré et al. 2024; T. O. Winterhalder et al. 2024). It has also exquisitely characterized many known directly imaged giant planets and brown dwarf companions (GRAVITY Collaboration et al. 2019, 2020; J. Kammerer et al. 2021; S. Lacour et al. 2021; J. J. Wang et al. 2021b; S. Blunt et al. 2023; W. O. Balmer et al. 2023; W. O. Balmer et al. 2024; E. Nasedkin et al. 2024b).

GRAVITY provides the most precise relative astrometry of directly detected planets yet measured, as well as K-band spectroscopy (in three modes, with $R = 50$, 500, and 5000). The K-band emission of substellar objects is shaped by absorption from H_2O, CO, and CH_4. The capability to conduct spectroscopy at close separations has enabled the precise estimation of the atmospheric abundances of a number of directly imaged planets (P. Mollière et al. 2020). GRAVITY's main limitation is its very small field of view (∼60 mas), which necessitates precise fiber pointing (and therefore some prior knowledge of the planet's position) to ensure that the planet's emission is coupled into the science fiber (see N. Pourré et al. 2024, for the characterization of the contrast performance of the techniques used in this paper and previous work).

The release of Gaia DR4 is expected to contain a list of astrometrically detected exoplanets,[24] which would provide prior knowledge on a large sample of planets that could be amenable to imaging with GRAVITY. Previous estimates of Gaia's exoplanet detection capabilities have indicated that as many as 21,000 long-period, giant exoplanets could be found over the mission's lifetime (M. Perryman et al. 2014). GRAVITY is expected to uniquely detect and characterize a subset of these astrometric planet candidates in young moving groups (N. Pourré et al. 2024; T. O. Winterhalder et al. 2024). This would open a unique window into atmospheric characterization of giant planets near their snowlines. The question then becomes, "to what degree do we expect to understand the orbits, atmospheric composition, and fundamental properties of planets that can only be detected (in the near term) with Gaia and GRAVITY?"

[24] https://www.cosmos.esa.int/web/gaia/release

1.3. AF Leporis b

Proper-motion anomalies between Hipparcos and Gaia (T. D. Brandt 2018; P. Kervella et al. 2019; T. D. Brandt 2021; P. Kervella et al. 2022) have been leveraged to directly image new companions with a higher detection rate than blind surveys (e.g., T. Currie et al. 2020; J. Chilcote et al. 2021; M. Bonavita et al. 2022; T. Currie et al. 2023; K. Franson et al. 2023a; Y. Li et al. 2023). Most notably, after uniform surveys in the decades prior had returned nondetections (B. A. Biller et al. 2013; J. M. Stone et al. 2018; E. L. Nielsen et al. 2019; R. Launhardt et al. 2020), proper-motion anomaly informed searches have uncovered a giant planet orbiting the young star AF Lep (HD 35850, HIP 25486, Gaia DR3 3009908378049913216) that has the lowest dynamically measured mass of any directly imaged exoplanet (K. Franson et al. 2023b; D. Mesa et al. 2023; R. J. De Rosa et al. 2023). The mass estimates for the planet at the time of discovery varied by about a Jupiter mass between data sets ($4.3^{+2.9}_{-1.2}$ $M_{\rm Jup}$, R. J. De Rosa et al. 2023; $3.2^{+0.7}_{-0.6}$ $M_{\rm Jup}$, K. Franson et al. 2023b; $5.237^{+0.085}_{-0.10}$ $M_{\rm Jup}$, D. Mesa et al. 2023), depending on the orbital coverage of the initial observations. The ensemble of discovery data was subsequently analyzed together, providing another estimate of the planet's dynamical mass ($2.8^{+0.6}_{-0.5}$ $M_{\rm Jup}$; Z. Zhang et al. 2023). The planet was recovered in archival observations dating back to 2011 using explainable machine learning assisted starlight subtraction, which significantly extended the baseline of the planet's measured orbital motion and constrained the orbit to low eccentricities (M. J. Bonse et al. 2024).

Initial estimates for the temperature and spectral type of the planet varied anywhere between 700 and 1200 K, placing the planet along the low surface gravity L/T transition, where spectral modeling is particularly challenging (M. S. Marley & T. D. Robinson 2015). Nevertheless, by combining the suite of discovery spectrophotometry, two studies have indicated that the planet appears to have a temperature between 700 and 900 K and an atmosphere that is enriched in metals compared to the solar value (Z. Zhang et al. 2023; P. Palma-Bifani et al. 2024). The planet was directly imaged at 4.4 μm using JWST/NIRCam coronagraphy, and the suppression of its flux at these wavelengths provided strong evidence that its atmosphere is in chemical disequilibrium (K. Franson et al. 2024). It has been suggested that the luminosity and dynamical mass of the planet are consistent with a delayed formation (that is, formation a few megayears after the host star formation; K. Franson et al. 2023b; Z. Zhang et al. 2023; Z. Zhang 2024).

The sensitivity of the planet's dynamical mass estimate to the viewing geometry, as well as the relatively unconstrained methane abundance given the wavelength coverage of existing observations, motivated our follow-up of this system with VLTI/GRAVITY.

Here we present the results of our new interferometric observations of AF Lep b with VLTI/GRAVITY. Relative astrometry at $\sim$50 μas precision near periastron constrains the low eccentricity of the planet's orbit with a time baseline of only 2 months and, coupled with the archival recovery of the planet near apoastron, places a strong upper limit on the eccentricity. The system provides an example of the excellent orbital precision that could be expected for planets detected astrometrically by Gaia and directly confirmed by GRAVITY. The *K*-band spectrum of the planet shows prominent methane absorption features that constrain the temperature, composition, and chemical disequilibrium of the atmosphere. We discuss future improvements necessary to better characterize the planet's atmosphere and bulk properties. We argue that the current ensemble of results is consistent with expectations from core accretion formation models. We conclude by looking forward to anticipated observations of Gaia-discovered planets with VLTI/GRAVITY.

2. Observations and Data Reduction

2.1. VLTI/GRAVITY

We observed AF Lep b the nights of UT 2023 November 2, UT 2023 November 24, and UT 2023 December 24 using the GRAVITY instrument (GRAVITY Collaboration et al. 2017) at the European Southern Observatory (ESO) Very Large Telescope Interferometer (VLTI). We used the four 8.2 m Unit Telescopes (UTs) and the dual-field mode of GRAVITY. The fringe tracker (S. Lacour et al. 2019; M. Nowak et al. 2024a), used to maintain the stability of the interferometric observables, was placed at the location of the host star, while the science fiber was placed at the predicted location of the planet and integrated to detect its fringe pattern. Our observation on 2023 November 2 was taken in off-axis mode and was complemented with an observation of the binary HD 25535 AB to calibrate the phase of the coherent flux (M. Nowak et al. 2024b) and with a single-field on-axis observation of the host star to calibrate the amplitude. Our observations on 2023 November 24 and 2023 December 24 were taken in on-axis mode, moving the science fiber periodically between the host star and the planet. The on-star observations were used to calibrate both the phase and the amplitude of the coherent flux, meaning that no observation of a separate calibrator was required. Conditions on 2023 November 2 were rather poor (seeing = 1.″1–1.″9) while conditions on 2023 November 24 and 2023 December 24 were good (seeing = 0.″4–0.″8). Our predictions for the location of the planet were based on all previously available relative astrometry,[25] and they achieved photon coupling efficiencies into the single mode fiber of $\gamma > 0.98$. This coupling efficiency is an analytic estimate of the throughput of the source depending on the displacement between the source and the center of the science fiber, and a derivation is given in Appendix A of J. J. Wang et al. (2021b). Table 1 records our observing log.

The raw data were reduced using the Public Release 1.5.0 (2021 July 1[26]) of the ESO GRAVITY pipeline (V. Lapeyrere et al. 2014), up to the "astroreduced" intermediate data products, in which individual detector integrations are not averaged, which helps to take full advantage of the sky rotation to deconvolve the planet signal from the residual starlight. The coherent flux of the science channel was first phase-referenced to the fringe tracker coherent flux and then corrected for the metrology zero-point, extracted either from the HD 25535 AB observation (for the dual-field off-axis observation of 2023 November 2) or from the on-star observations (for the dual-field on-axis observations of 2023 November 2 and 2023 November 24).

[25] We fit 10,000 orbits to the available relative astrometry of the planet ahead of each observation using the Orbits For The Impatient (OFTI) algorithm via the `orbitize!` package (S. Blunt et al. 2017, 2020). We then predicted the location of the planet during a given week of VLTI UT runs based on these orbits.

[26] https://www.eso.org/sci/software/pipelines/gravity

Table 1
Observing Log

Date (UT)	Target		NEXP/NDIT/DIT		Air Mass	τ_0	Seeing	Fiber Pointing (ΔR.A./Δdecl.)	γ
	SC	FT	SC	FT					
2023-11-02	HD 25535 A/B	HD 25535 B/A	4/64/1 s	4/64/1 s	1.03–1.06	2.4–3.0 ms	1.″09−1.″40	718.32/803.6	0.999
2023-11-02	AF Lep b	AF Lep A	14/4/100 s	2/64/1 s	1.03–1.09	1.6–2.4 ms	1.″12−1.″92	316.5/64.3	0.999
2023-11-24	AF Lep b	AF Lep A	18/12/30 s	5/16/3 s	1.03–1.15	4.8–13.8 ms	0.″41−0.″76	319.71/57.54	0.988
2023-12-24	AF Lep b	AF Lep A	23/12/30 s	4/48/1 s	1.03–1.31	6.4–11.5 ms	0.″41−0.″68	315.38/55.84	0.999

Note. Science Camera (SC) and Fringe Tracker (FT) targets and exposures are recorded. NEXP, NDIT, and DIT denote the number of exposures, the number of detector integrations per exposure, and the detector integration time, respectively. Parameter τ_0 denotes the atmospheric coherence time. The fiber pointing is the placement of the science fiber relative to the fringe tracking fiber (which is placed on the central star), and γ is the coupling efficiency at the position of the companion, depending on the distance between pointing and planet location (see Table 2).

We measured the position ($\Delta\alpha$, $\Delta\delta$) and contrast spectrum ($C_{\rm planet}$) of the companion relative to its bright host star from the phase-referenced complex coherent fluxes. We used the `exogravity` pipeline,[27] following GRAVITY Collaboration et al. (2019) and subsequent ExoGRAVITY work (see in particular GRAVITY Collaboration et al. 2020; M. Nowak et al. 2020, 2024b). In the absence of the stellar halo, instrumental throughput, or Earth's atmosphere, the planet's coherent flux $\Gamma_{\rm planet}(b, t, \lambda)$ is described by the baseline b, exposure t, and wavelength λ:

$$\Gamma_{\rm planet}(b, t, \lambda) = C_{\rm planet}(\lambda)\Gamma_{\rm star}(b, t, \lambda) \times e^{-i\frac{2\pi}{\lambda}(\Delta\alpha\times U(b,t)+\Delta\delta\times V(b,t))}, \quad (1)$$

where $\Gamma_{\rm star}$ is the stellar coherent flux and $U(b, t)$ and $V(b, t)$ are the u-v plane coordinates for a given baseline and exposure time, respectively. We can model the measured coherent fluxes in the presence of a bright host, instrumental throughput, and atmospheric transmission, $\Gamma_{\rm on\ planet}(b, t, \lambda)$, as a combination of the transmission function G, a low-order polynomial Q, the stellar coherent flux $\Gamma_{\rm star}$, and planet coherent flux $\Gamma_{\rm planet}$:

$$\Gamma_{\rm on\ planet}(b, t, \lambda) = Q(b, t, \lambda)G(b, t, \lambda)\Gamma_{\rm star}(b, t, \lambda) + G(b, t, \lambda)\Gamma_{\rm planet}(b, t, \lambda). \quad (2)$$

The intermittent observations of the star using the science fiber give us a measure of G, $\Gamma_{\rm star}$, and allow us to measure $\Gamma_{\rm on\ planet}$ in terms of the contrast spectrum, the ratio of the planet and stellar spectrum, canceling out G if we assume that G is stable across the Δt between on-planet and on-star observations. In reality, the change in the atmospheric transmission across Δt induces small telluric features in our final spectrum that result in additional correlated noise, which future work could address.

These equations are nonlinear in ($\Delta\alpha$, $\Delta\delta$) but not in $C_{\rm planet}$, so we first begin by solving for ($\Delta\alpha$, $\Delta\delta$) by assuming $C_{\rm planet}$ based on our reproduction of the best-fitting `petitRADTRANS` model in Z. Zhang et al. (2023). Using the matrix form $\mathbf{\Gamma}_{\rm on\ planet} = (\Gamma_{\rm on\ planet}(b, t, \lambda))_{b,t,\lambda}$, we define a χ^2:

$$\chi^2(\Delta\alpha, \Delta\delta, Q, C_{\rm planet}) = [\Gamma_{\rm on\ planet} - \Gamma_{\Delta\alpha,\Delta\delta,Q,C_{\rm planet}}]^T \times W^{-1}[\Gamma_{\rm on\ planet} - \Gamma_{\Delta\alpha,\Delta\delta,Q,C_{\rm planet}}], \quad (3)$$

where W is the covariance matrix on the projected coherent fluxes $\tilde{\mathbf{\Gamma}}$ (see M. Nowak et al. 2020, Appendix A.4). A Bayes factor is then constructed by taking $\chi^2_{\rm reference} = \chi^2(0, 0)$, where the exponential is flat and there is no planet signal. This quantity, $z(\Delta\alpha, \Delta\delta) = \Delta\chi^2 = \chi^2_{\rm reference} - \chi^2(\Delta\alpha, \Delta\delta)$, can be computed for any $\Delta\alpha$, $\Delta\delta$, but we restrict the computation to the effective field of view of the instrument. We calculate $\Delta\chi^2$ on a 200×200 grid about the 30 mas field of view defined by the fiber's pointing and the FWHM of the fiber's throughput curve (J. J. Wang et al. 2021b, Appendix A). Figure 1 shows these detection maps in terms of the reduced $\Delta\chi^2_{\rm red}$ for the three observations, which all result in strong detections of AF Lep b. We take the minimum of the $\Delta\chi^2$ map as the preliminary companion position and then calculate another 200×200 step grid with a range restricted to ± 2.5 mas around the initial $\Delta\chi^2$ grid minimum (that is, zooming into the central "peak" of the $\Delta\chi^2$ map). This minimum is used to initialize a gradient descent algorithm that determines the $\Delta\alpha$, $\Delta\delta$ best describing the companion's position given the data. The procedure is repeated for each of the individual exposures of each night. The final measurement and associated covariance matrix are taken to be the mean and covariance of the individual measurements, following M. Nowak et al. (2020, 2024a). This way, the uncertainty is derived from the data themselves and not, for instance, the relatively arbitrarily defined grid on which the $\Delta\chi^2$ maps are computed, or the uncertainty reported by the gradient descent algorithm, which may underestimate the true uncertainty. This astrometry is recorded in Table 2.

One the astrometry is determined, the contrast spectrum and its covariance matrix can be extracted using a joint fit of the coherent flux obtained on all of the baselines and individual detector integrations, holding the astrometry constant. We find that the conditions and observing strategy for the observation on 2023 November 2 result in a spectrum of significantly worse quality than the observations on 2023 November 24 and 2023 December 24; this spectrum has much larger uncertainties compared to the later two observations and does not contribute much information when the three are combined with a weighted median. We therefore use a weighted median combination of the two on-axis spectra (and their associated covariance matrices) from 2023 November 24 and 2023 December 24 for our final analysis. We transformed the contrast spectrum of the companion into a flux-calibrated spectrum using a synthetic spectrum of the host star. We scaled a `BT-NextGen` (F. Allard et al. 2011) spectrum with $T_{\rm eff} = 6000$ K, $\log(g) = 4.3$, and [Fe/H] $= -0.27$ (Z. Zhang et al. 2023) to archival photometry from Gaia (Gaia Collaboration et al. 2023), Tycho2 (E. Høg et al. 2000), and the Two Micron All Sky Survey (R. M. Cutri et al. 2003) using `species`

[27] https://gitlab.obspm.fr/mnowak/exogravity

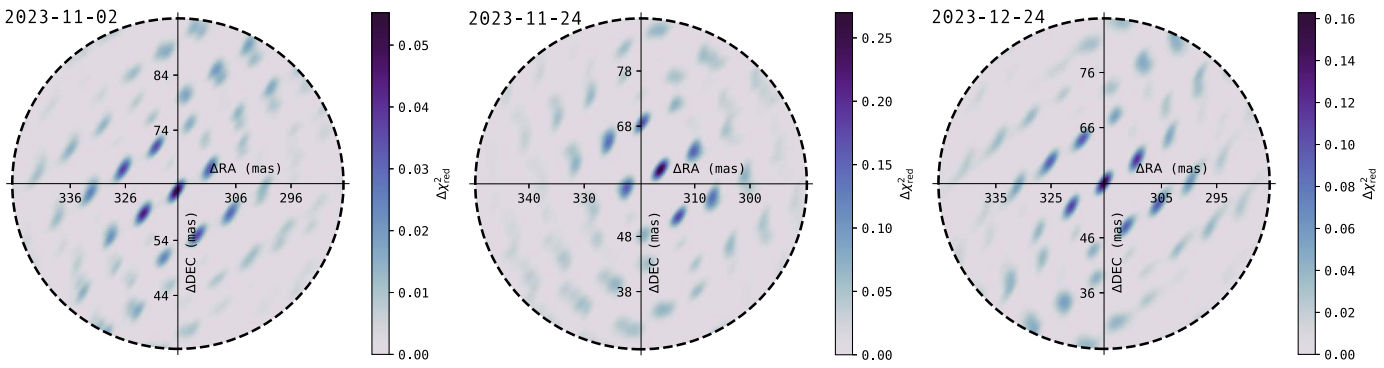

Figure 1. Detections of AF Lep b within the VLTI/GRAVITY fiber field of view. Each panel visualizes the $z_{red} = \Delta\chi^2_{red}$ calculated for various positions (ΔR.A. and Δdecl. in milliarcseconds, i.e., the displacement with respect to the measured position of the host star AF Lep A), fitting the interferometric observables with a polynomial model of the transmission and stellar halo contribution and a coherent point source with the spectral signature of a T dwarf. Each epoch is presented chronologically, left to right: 2023 November 2, 2023 November 24, and 2023 December 24. The dashed black circle indicates the effective fiber field of view, ∼60 mas. The origin is the placement of the science fiber on-sky for a given observation, a prediction based on the previous available orbit fit. The strongest peak in the χ^2 map reveals the position of the companion, with lower likelihood peaks surrounding this central peak. The shape and distribution of the likelihood depend on the *u*-*v* plane coverage of the observations.

Table 2
Relative Astrometry of AF Lep b from VLTI/GRAVITY

Date (UT)	Epoch (MJD)	ΔR.A. (mas)	$\sigma_{\Delta\alpha}$ (mas)	ΔDecl. (mas)	$\sigma_{\Delta\delta}$ (mas)	ρ
2023-11-02	60251.32	316.89	0.07	62.91	0.09	−0.73
2023-11-24	60273.22	316.26	0.04	60.17	0.04	−0.82
2023-12-24	60302.21	315.44	0.05	55.93	0.05	−0.55

Note. The covariance matrix for each measurement can be reconstructed using $\sigma^2_{\Delta\alpha}$ and $\sigma^2_{\Delta\delta}$ on the diagonal and $\rho \times \sigma_{\Delta\alpha} \times \sigma_{\Delta\delta}$ on the off-diagonal.

(T. Stolker et al. 2020). We sampled this scaled model spectrum on the GRAVITY wavelength grid using `spectres` (A. C. Carnall 2017). Our final flux-calibrated *K*-band spectrum of AF Lep b is shown in Figure 2, alongside previous observations. We find that our spectrum agrees well with the observed SPHERE K1 and K2 photometry (see next section).

2.2. Previous Observations

For our spectral analysis, we re-reduced the two pupil tracking, angular differential imaging (ADI) mode observations on 2022 October 16 and 2022 December 20 presented in D. Mesa et al. (2023) to achieve a higher signal-to-noise ratio (SNR) spectrum by leveraging the `PACO` algorithm. The re-reduction was computed on the COBREX Data Center, a modified and improved server based on the High Contrast Data Center (HC-DC, formerly known as the SPHERE Data Center; P. Delorme et al. 2017). Since the SPHERE observations on 2022 October 20 were taken in the star hopping reference differential imaging mode (Z. Wahhaj et al. 2021; R. J. De Rosa et al. 2023) and have a significantly lower integration time and higher air mass than the ADI observations, we do not re-reduce them or use them in our spectral analysis, as that would involve fitting flux (and potentially wavelength calibration) offset parameters during the atmospheric modeling step (Z. Zhang et al. 2023; P. Palma-Bifani et al. 2024). The pre-reduction steps consisting of dark, flat, distortion, and bad pixel corrections are based on the SPHERE data reduction and handling (DRH) pipeline provided by ESO (A. Pavlov et al. 2008). A few additional customs steps were added for the IFS pre-reduction to the DRH, mainly to correct the crosstalk during the spectral extraction and improve the bad pixel correction (D. Mesa et al. 2015).

We post-processed the data using the `robust PACO ASDI` algorithm (O. Flasseur et al. 2018, 2020b, 2020a). `PACO` estimates the nuisance component using a multi-Gaussian model at a local scale on small patches, allowing for a better estimation of the temporal and spectral correlation of the nuisance. Details on the improvements of the pre-reduction pipeline, the optimization regarding the ASDI mode of `PACO`, and the obtained performances can be found in A. Chomez et al. (2023). `PACO` provides a contrast gain between 1 and 2 mag at all separations, as well as reliable and statistically grounded SNR detection and contrast maps in an unsupervised and data-driven fashion. The two extracted spectra are averaged to produce the spectrum shown in Figure 2.

In our spectral analysis we also include a weighted average of the Keck/NIRC2 *L'* photometry from K. Franson et al. (2023b, 2024) and the JWST/NIRCam F444W photometry from K. Franson et al. (2024).

3. Analysis

3.1. Orbital Analysis

In order to determine the architecture of the AF Lep system, we fit the observations with two-body Keplerian orbits using `orvara` (T. D. Brandt 2021). This code was chosen because it has been predominately used in previous studies of the system (R. J. De Rosa et al. 2023; K. Franson et al. 2023b; D. Mesa et al. 2023; Z. Zhang et al. 2023; M. J. Bonse et al. 2024). The orbit fits included our new GRAVITY observations, the literature relative astrometry available prior to our observations,[28] the absolute astrometry of the system from the HGCA, and the HIRES RV observations of the star (R. P. Butler et al. 2017).

Our `orvara` runs use the `ptemcee` sampler (D. Foreman-Mackey et al. 2013; W. D. Vousden et al. 2016) with 20 temperatures, 1000 walkers, and 500,000 steps per walker and were thinned to only save every 100th step; we visually

[28] The two epochs of SPHERE astrometry from D. Mesa et al. (2023), the single epoch of SPHERE astrometry from R. J. De Rosa et al. (2023), the Keck/NIRC2 *L'* astrometry from K. Franson et al. (2023b), and the recently recovered archival VLT/NACO *L'* astrometry from M. J. Bonse et al. (2024).

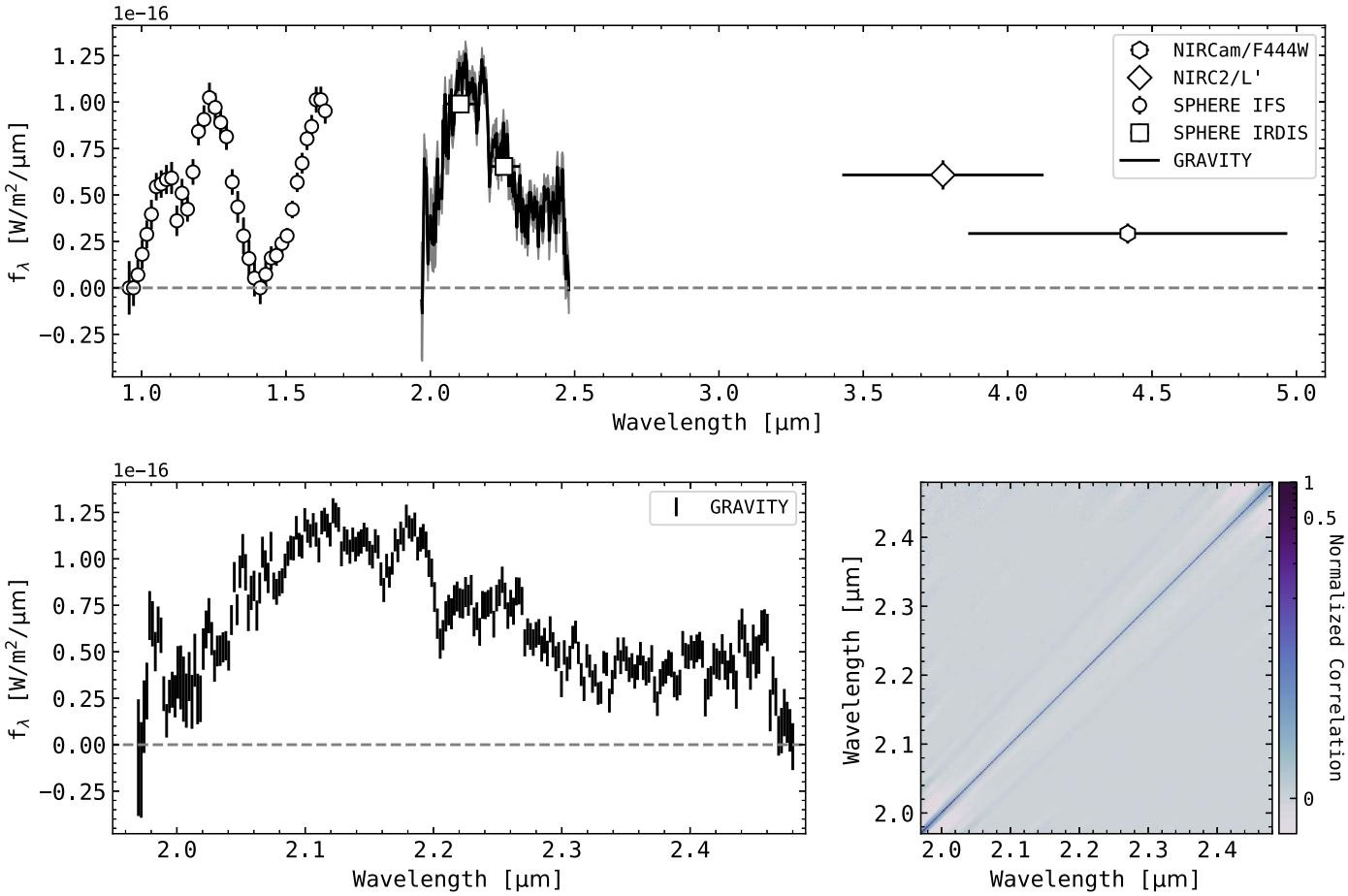

Figure 2. SED of AF Leporis b in the context of new GRAVITY observations. The top panel plots our reprocessed SPHERE IFS (small circles) and IRDIS (squares) spectrophotometry (see Section 2.2), Keck/NIRC2 Lp photometry from K. Franson et al. (2023a, 2024; large circle), and JWST/NIRCam F444W photometry from K. Franson et al. (2024; hexagon), alongside the GRAVITY spectrum from this work (line). The bottom left panel plots the GRAVITY spectrum as error bars with uncertainties corresponding to the square root of the diagonal of the covariance matrix. The spectrum is dominated by methane absorption from 2.2 to 2.4 μm; there is correlated noise lurking beneath the prominent molecular absorption features. The bottom right panel plots the empirical covariance matrix of the GRAVITY spectrum, in terms of the maximum value of the matrix, with a log stretch in order to illustrate the small but nonzero off-axis correlation terms. These are accounted for in all the spectral analyses in this paper. The new SPHERE and GRAVITY spectra are available as the data behind the figure.

(The data used to create this figure are available in the online article.)

inspected the chains for convergence and discarded the first 3000 saved steps (so the first 60% of each chain) as "burn-in." We fit for the mass of AF Lep A, the mass of AF Lep b, the orbit semimajor axis (a), parameterized forms of the eccentricity and argument of periastron ($\sqrt{e}\cos(\omega_\star)$, $\sqrt{e}\sin(\omega_\star)$), the inclination angle (i), the longitude of the ascending node (Ω), the mean longitude at the reference epoch 2010 January 1 ($\lambda_{\rm ref}$), the system parallax (ϖ), and RV zero-point and jitter terms. We adopt uninformative priors on all parameters (see T. D. Brandt 2021), except for the system parallax (we adopt the Gaia DR3 parallax as a Gaussian prior) and the primary mass (we adopt $\mathcal{N}(1.20, 0.06)M_\odot$; K. Franson et al. 2023b). The $\sqrt{e}\cos(\omega_\star)$, $\sqrt{e}\sin(\omega_\star)$, eccentricity, and argument of periastron parameterization is used to address a known bias in sampling circular orbits with eccentricity as a free parameter (L. B. Lucy & M. A. Sweeney 1971; N. L. Zakamska et al. 2011). Table 3 records the results of this fit, while Figure 3 illustrates them. The posterior distribution of key parameters is shown in Figure 4.

This updated fit represents a significant improvement in the constraints on the planet's orbit. We note here that the majority of previous work has been unable to accurately constrain the circular nature of the planet's orbit given the precision of the data and limited coverage of the planet's orbital arc since its discovery. This resulted in orbit fits with posterior distributions of eccentricity dominated by the uniform prior distribution (this effect has been detailed most recently in S. Blunt et al. 2023), with e ranging from ~0.5 (D. Mesa et al. 2023) to ~0.2 (K. Franson et al. 2023b). The recovery of the planet in archival Very Large Telescope (VLT)/NACO data (M. J. Bonse et al. 2024) recently facilitated a likelihood-dominated orbit fit, which indicated an upper limit on $e < 0.06$, 0.15, and 0.26, at 1σ, 2σ, and 3σ, respectively. Compared to this previous orbit fit, our fit sets the limit at $e < 0.02$, 0.07, and 0.13 at 1σ, 2σ, and 3σ, respectively. We discuss the implications of these constraints in Section 4.1.

3.2. Atmospheric Analysis

3.2.1. Evolutionary Model Predictions

AF Lep b has been and will continue to be studied intently in the context of evolutionary modeling as its parameters are refined (R. J. De Rosa et al. 2023; K. Franson et al. 2023b; D. Mesa et al. 2023; Z. Zhang et al. 2023; R. Gratton et al. 2024; P. Palma-Bifani et al. 2024). Within the year since its discovery, the specific estimates of its bulk properties as

Table 3
Orbital Analysis of AF Lep A+b with `orvara`

Parameter	Prior	Median and 1σ CI
Fitted Parameters		
Primary mass $M_{\rm pri}$ ($M_\odot$)	$\mathcal{N}(1.20, 0.06)$	$1.22^{+0.03}_{-0.04}$
Secondary mass $M_{\rm sec}$ ($M_{\rm J}$)	$1/M$ (log-flat)	3.75 ± 0.5
Semimajor axis a (au)	$1/a$ (log-flat)	$8.98^{+0.15}_{-0.08}$
$\sqrt{e}\sin\omega$	uniform	-0.03 ± 0.12
$\sqrt{e}\cos\omega$	uniform	$0.00^{+0.08}_{-0.08}$
Inclination i (deg)	$\sin(i)$, $0° < i < 180°$	$57.5^{+0.6}_{-0.7}$
Mean longitude at 2010.0 $\lambda_{\rm ref}$[a] (deg)	uniform	$171.8^{+2.1}_{-1.6}$
Ascending node Ω (deg)	uniform	$68.8^{+0.4}_{-0.7}$[b]
Parallax ϖ (mas)	$\mathcal{N}$(Gaia DR3)	37.254 ± 0.019
System proper motion in R.A. μ_α (mas yr^{-1})	uniform	17.13 ± 0.01
System proper motion in decl. μ_δ (mas yr^{-1})	uniform	-49.20 ± 0.01
RV zero-point RV_0 (m s^{-1})	uniform	-10 ± 2
RV jitter $\sigma_{\rm jit}$ (m s^{-1})	$1/\sigma$ (log-flat)	175^{+38}_{-29}
Derived Parameters		
Period (yr)	⋯	$24.3^{+0.9}_{-0.4}$
Argument of periastron ω (deg)	⋯	289^{+13}_{-21}[b]
Eccentricity e	⋯	$0.013^{+0.024}_{-0.010}$[c]
Semimajor axis a (mas)	⋯	$334.4^{+5.6}_{-2.9}$
Time of periastron $T_0 = t_{ref} - P\frac{\lambda-\omega}{360°}$ (JD)	⋯	24580^{+4200}_{-1300}
Mass ratio	⋯	$0.00294^{+0.00036}_{-0.00036}$

Notes.
[a] The reference epoch is $t_{\rm ref} = 2455197.5$ JD ($\lambda_{\rm ref}$; 2010 January 1 00:00 UT).
[b] Degenerate solution, with values $\pm 180°$, so there exists a second population of orbits with $\Omega = 248^{+0.4}_{-0.7}°$, $\omega = 109^{+13}_{-21}°$, $\lambda^*_{\rm ref} = 351.8^{+2.1}_{-1.6}°$ in the posterior distribution.
[c] The marginalized posterior distribution on eccentricity encompasses 0.0. This is effectively an upper limit, $e < 0.02$, 0.07, and 0.13 at 1σ, 2σ, and 3σ, respectively.

predicted by evolutionary models have varied widely because of the systematic uncertainty in the estimates of its dynamical mass (see Section 4.1). There are also systematic uncertainties in the age estimate for the β-Pictoris moving group (see discussion in J. Lee & I. Song 2024), but given the generally adopted isochronal age of 24 ± 3 Myr (C. P. M. Bell et al. 2015), previous work has converged on a rough range of bulk parameters for the planet, namely effective temperatures 700–850 K, surface gravities of $\log(g) \sim 3.7$, and radii of about $R \sim 1.3 R_{\rm J}$. In general, we expect that, regardless of initial entropy, the planet's radius will not be smaller than $1.1 R_{\rm J}$ at an age less than a few hundred million years (M. S. Marley et al. 2012), and certainly no less than about $0.9 R_{\rm J}$ at any age (e.g., Figure 3 in A. Burrows et al. 2001). As the goal of this paper is to assess primarily the orbit and atmosphere of the planet in the context of its formation, we limit our evolutionary model analysis to that which will help contextualize our atmospheric analysis (see Table 3 and Figure 3 in Z. Zhang et al. 2023, which consider a wide variety of evolutionary models—we adopt their evolutionary-model-based priors in the sections below). We used `species` to linearly interpolate the hybrid-cloudy evolutionary model grid from D. Saumon & M. S. Marley (2008) to establish a general range of expected planetary effective temperatures, surface gravities, radii, and luminosities given the dynamical mass and isochronal moving group age. We find that $M_b = 3.75 \pm 0.5\, M_{\rm J}$ and 24 ± 3 Myr imply $T_{\rm eff} = 770 \pm 75$, $\log(g) = 3.73 \pm 0.06$, $R = 1.30 R_{\rm J} \pm 0.01 R_{\rm J}$, and $\log(L/L_\odot) = -5.26 \pm 0.18$. These are recorded in Table 4.

3.2.2. Self-consistent Atmospheric Models

We perform initial reconnaissance of the atmospheric properties of AF Lep b using precomputed grids of self-consistent radiative–convective equilibrium (RCE) models. We compared the GRAVITY spectrum to the modern, cloudless `Sonora Bobcat` (M. S. Marley et al. 2021) and `Sonora Elf Owl` (S. Mukherjee et al. 2024) grids, the former being a solar-abundance, rainout chemical equilibrium model and the latter varying abundances in terms of metallicity and C/O ratio, in addition to including the effects of disequilibrium chemistry by transport-induced mixing by parameterizing the Eddy diffusion coefficient $\log(K_{zz})$. Neither of these cloudless models reproduces the Y- or J-band flux of the object; they predict bluer spectra than are observed. We compared the full spectral energy distribution (SED) of the object to the cloudy, solar-abundance `BT-Settl` model grid (F. Allard et al. 2011), which resulted in a poor fit to the SPHERE and GRAIVTY spectra. We primarily focus our discussion on the `Exo-REM` forward model grid (J. L. Baudino et al. 2015; B. Charnay et al. 2018). This model parameterizes nonequilibrium chemistry between C-, N-, and O-bearing molecules with profiles of the eddy diffusion coefficient that vary with pressure determined for each grid point, and it parameterizes the cloud particle distribution using a simplified microphysical treatment that produces cloud particle radii intermediate to the fixed radius or fixed sedimentation parameter case. The publicly available grid[29] varies temperature ($T_{\rm eff}$), surface gravity ($\log(g)$), carbon-to-oxygen ratio (C/O), and metallicity compared to solar ([M/H]). The grid varies temperature between 400 and 2000 K in steps of 50 K, surface gravity between 3.5 and 5.0 in steps of 0.5, [M/H] between −0.5 and 2 (0.3 and 100 times solar) in steps of 0.5, and C/O between 0.1 and 0.8 in steps of 0.05. A previous version of this grid was used by P. Palma-Bifani et al. (2024), who found that the existing SPHERE data sets and L'-band photometry were best fit by enriched metallicity (>0.4) models; their grid did not include the highest-metallicity grid points ([M/H] ∈ [1, 2], however. The updated version of the grid we use here encompasses the high-metallicity solutions found in the retrieval analysis in Z. Zhang et al. (2023) and K. Franson et al. (2024).

We use `species` to linearly interpolate the spectra between grid points and compare our data to the model. In our fitting routine, we sample the grid parameters, parallax (which determines the absolute flux of the model along with planetary radius), and, motivated by the presence of residual correlated noise in our SPHERE spectrum (e.g., J. P. Greco & T. D. Brandt 2016), a Gaussian process parameterized by a squared-exponential kernel as an estimate for said correlated noise (see Equation (4) in J. J. Wang et al. 2020). The empirical GRAVITY correlation matrix (computed in Section 2.1) is included in our likelihood function. We used `pyMultiNest`[30] (F. Feroz & M. P. Hobson 2008; F. Feroz et al. 2009;

[29] https://lesia.obspm.fr/exorem/YGP_grids/
[30] https://johannesbuchner.github.io/PyMultiNest/

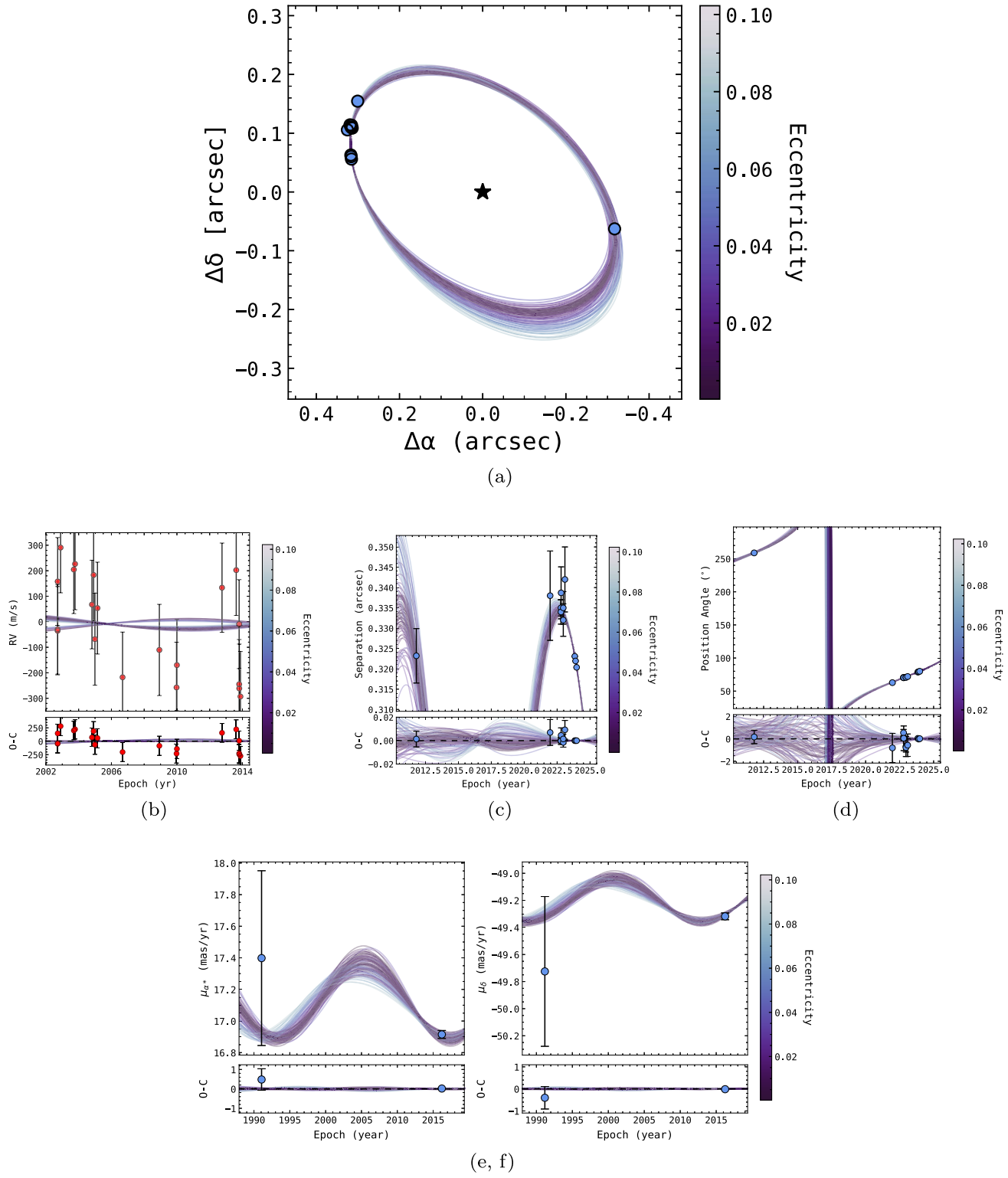

Figure 3. Two-body orbits fit to the observations of the AF Lep system. (a) Sky-projected relative astrometry of AF Lep b (blue scatter points) and fit orbits (lines, color-coded by eccentricity). The new high-precision VLTI/GRAVITY relative astrometry constrains the eccentricity and inclination of the orbit and, when coupled with the long time baseline of the VLT/NACO recovery (M. J. Bonse et al. 2024), results in a well-known, circular orbit. (b) Keck/HIRES RV measurements of AF Lep A and the best-fitting orbits. The available RVs do not constrain the orbit fit, and there remain two degenerate solutions for the argument of periastron (ω) and longitude of ascending node (Ω). (c) Projected separation vs. time for each orbit, and relative astrometry. There is larger scatter between single mirror instruments, but these are consistent within 1σ with the best-fitting circular orbits that are driven by the GRAVITY astrometry. (d) Likewise, for the position angle vs. time for each orbit and the relative astrometry. (e, f) The proper motions in R.A. and decl. for AF Lep A (blue scatter points) and the reflex motion due to the orbit of AF Lep b (colored lines).

J. Buchner et al. 2014) to sample the interpolated grid with 500 live points. We place a Gaussian prior on the parallax based on the Gaia DR3 measurement (Gaia Collaboration et al. 2023). Following P. Palma-Bifani et al. (2024), when fitting the `Exo-REM` grid we attempted to place a prior on $\log(g) \sim 3.7$ informed by the dynamical mass and evolutionary model

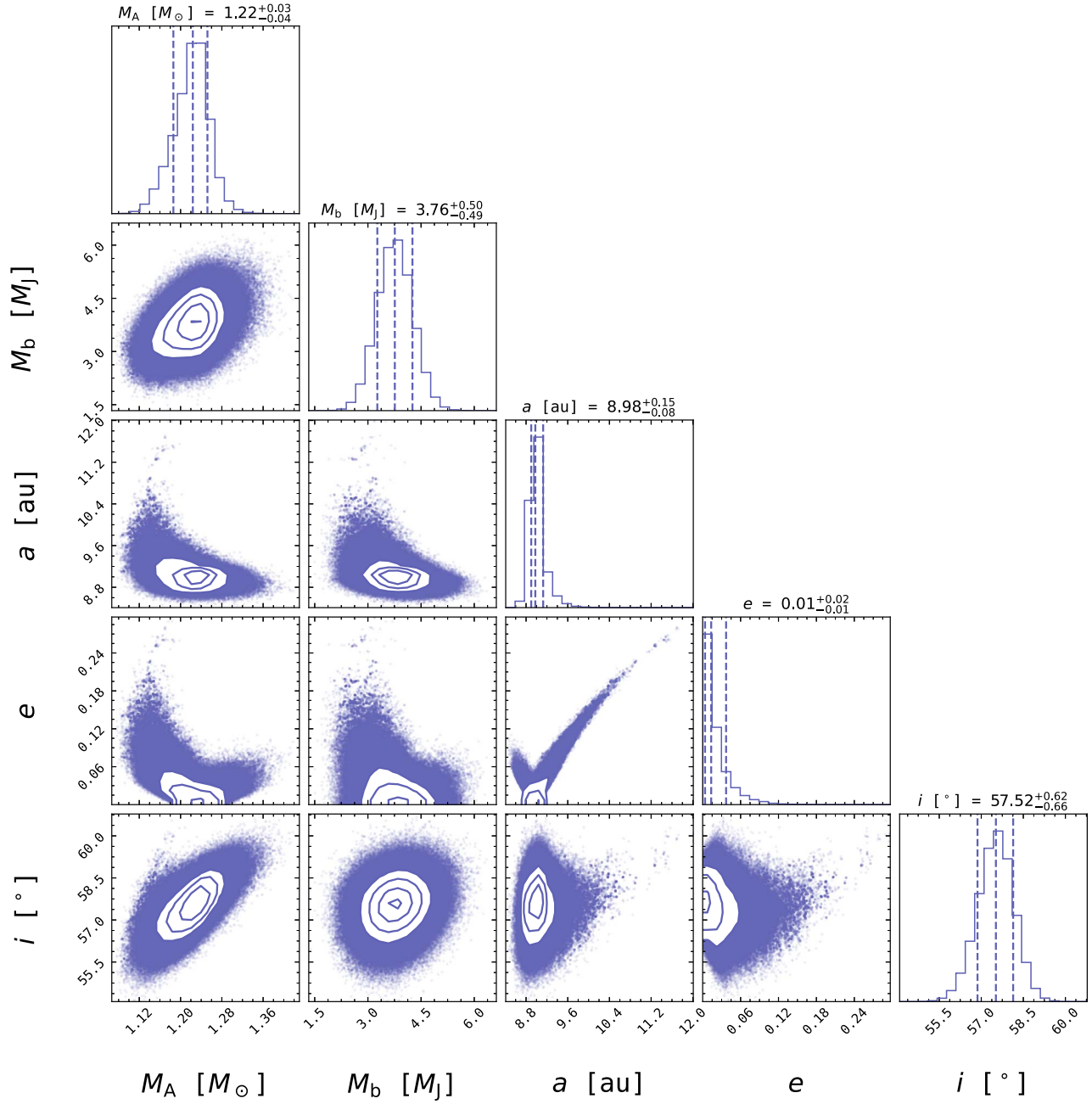

Figure 4. Posterior distribution of select parameters from the `orvara` orbit fit visualized in Figure 3 and summarized in Table 3. Complex correlations are apparent between a and e that result in a low-probability tail of more eccentric orbits. The majority of accepted orbits are circular. The component masses are well-constrained, roughly normal distributions.

predictions for the radius, but we found that any prior that reasonably captured the systematic uncertainty in the evolutionary radius (e.g., ± 0.1 dex) was always driven away from the prior. We therefore compare posteriors fixing the $\log(g) = 3.7$ and mass to $M_b = 3.75 M_{\rm Jup}$ versus setting a Gaussian prior equivalent to our dynamical mass estimate on the mass ($M_b = 3.75 M_{\rm Jup} \pm 0.5 M_{\rm Jup}$) and letting radius and $\log(g)$ vary freely.

Table 4 records the results from this grid interpolation fit comparison. Figure 5 compares our new GRAVITY spectrum to the `Sonora` models, `Exo-REM` model, and `petitRADTRANS` agnostic cloud retrievals (see next section). Figure 6 compares the results of the `Exo-REM` models fit to the full data set. The results of these model comparisons are discussed in Section 4.4.

3.2.3. An Initial Analysis Using Atmospheric Retrievals

We investigated the atmospheric composition of AF Lep b by sampling thousands of parameterized model spectra, commonly referred to as an atmospheric retrieval (N. Madhusudhan 2018). In this framework, we parameterize the pressure–temperature (P–T) structure of the atmosphere, the chemical abundances, the clouds, and the bulk properties of the atmosphere, in order to facilitate the rapid calculation of model spectra that are compared to our data, so that we can sample the

Table 4
Subset of Parameters for AF Lep b Derived from Evolutionary and Atmospheric Analysis

Model	Notable Model Parameters								$\chi^2_{\rm red.}$/d.o.f.
	Mass (M_J)	$T_{\rm eff}$ (K)	log(g)	Radius (R_J)	[Fe/H]	C/O	$\log(K_{zz})/P_{\rm quench}$ [a] [log(cm^2/s)]/[bars]	$\log(L/L_\odot)$	
Evolutionary									
SM08 (hybrid-cloudy), 24 ± 3 Myr	3.75 ± 0.5	770 ± 75	3.73 ± 0.06	1.30 ± 0.01	solar	solar	⋯	-5.26 ± 0.18	⋯
Self-consistent RCE grid interpolation[b]									
— Gravity spectrum only —									
`Sonora Bobcat`, $\mathcal{U}(0.5, 2.0)_{R_p}$	0.18 ± 0.02	1260 ± 4	3.25 ± 0.01	$0.50^{+0.01}_{...}$[c]	0.22 ± 0.02	⋯	⋯	-5.22 ± 0.01	3.90/228
`Sonora Elf Owl`, $\mathcal{U}(0.5, 2.0)_{R_p}$	3.02 ± 0.51	1080 ± 50	4.05 ± 0.15	0.82 ± 0.09	0.05 ± 0.03	$0.3^{+0.04}_{...}$[c]	7.73 ± 0.69	-5.06 ± 0.02	2.35/226
`Exo-REM`, $\mathcal{U}(0.5, 1.25)_{R_p}$[d]	3.53 ± 0.55	$836^{+7.5}_{-10}$	3.80 ± 0.10	$1.17^{+0.05}_{-0.03}$	0.63 ± 0.05	0.54 ± 0.03	⋯	-5.20 ± 0.01	2.16/227
`Exo-REM`, $\mathcal{U}(1.25, 2.0)_{R_p}$[d]	3.80 ± 0.45	762^{+16}_{-10}	$3.65^{+0.06}_{-0.08}$	$1.46^{+0.07}_{-0.05}$	0.66 ± 0.06	$0.48^{0.02}_{-0.04}$	⋯	-5.16 ± 0.02	2.15/227
— All data —									
`BT-Settl`, $\mathcal{U}(0.5, 2.0)_{R_p}$	4.21 ± 0.04	766 ± 2	$3.50^{+0.01}_{...}$[c]	1.81 ± 0.01	solar	solar	⋯	-4.97 ± 0.01	6.02/270
`Exo-REM`, $\mathcal{U}(0.5, 2.0)_{R_p}$	4.05 ± 0.46	845 ± 3	3.89 ± 0.05	1.13 ± 0.01	0.69 ± 0.02	0.57 ± 0.01	⋯	-5.21 ± 0.01	2.45/268
`Exo-REM`, $M_b = 3.75 M_{\rm Jup}$, $\log(g) = 3.7$	=3.75	783 ± 5	=3.7	1.35 ± 0.01	0.77 ± 0.03	0.49 ± 0.01	⋯	-5.18 ± 0.01	2.63/266
`petitRADTRANS` atmospheric retrieval[b]									
— Gravity spectrum only —									
Agno., Grad. *P–T*, free chem., $\mathcal{U}(0.5, 2.0)_{R_p}$	3.6 ± 0.4	851 ± 40	3.78 ± 0.14	$1.22^{+0.19}_{-0.14}$	⋯	0.43 ± 0.05	⋯	$-5.12^{+0.05}_{0.08}$	2.33/204
Agno., Grad. *P–T*, (dis)eq. chem., $\mathcal{U}(0.5, 2.0)_{R_p}$	3.65 ± 0.4	1113 ± 50	4.27 ± 0.08	0.70 ± 0.05	0.40 ± 0.11	0.50 ± 0.05	2.67 ± 0.06	-5.15 ± 0.03	2.31/212
— All data —									
Cloudless, spline *P–T*, (dis)eq. chem., $\mathcal{U}(0.5, 2.0)_{R_p}$	3.9 ± 0.4	947 ± 20	4.22 ± 0.05	0.76 ± 0.03	0.83 ± 0.08	0.61 ± 0.04	$2.59^{+0.10}_{-0.14}$	-5.33 ± 0.01	2.49/247
Agno., Grad. *P–T*, free chem., $\mathcal{U}(0.5, 2.0)_{R_p}$	3.7 ± 0.4	980 ± 25	4.22 ± 0.06	0.74 ± 0.03	⋯	0.56 ± 0.05	⋯	-5.32 ± 0.01	2.57/245
EddySed, three-part *P–T*, (dis)eq. chem., $\mathcal{U}(0.5, 2.0)_{R_p}$	3.9 ± 0.4	970 ± 14	4.23 ± 0.06	0.75 ± 0.03	0.79 ± 0.08	0.53 ± 0.04	2.28 ± 0.22	-5.33 ± 0.02	2.57/253
EddySed, Grad. *P–T*, free chem., $\mathcal{U}(0.5, 2.0)_{R_p}$	3.8 ± 0.3	972 ± 24	4.22 ± 0.06	0.75 ± 0.04	⋯	0.52 ± 0.04	⋯	-5.31 ± 0.02	2.47/244
EddySed, Grad. *P–T*, (dis)eq. chem., $\mathcal{U}(0.5, 2.0)_{R_p}$	3.8 ± 0.4	947 ± 19	4.17 ± 0.06	0.80 ± 0.04	0.74 ± 0.09	0.50 ± 0.04	2.84 ± 0.05	-5.32 ± 0.01	2.42/252
EddySed, Grad. *P–T*, (dis)eq. chem., $\mathcal{U}(1.2, 1.5)_{R_p}$	4.1 ± 0.3	789 ± 9	3.82 ± 0.04	$1.23^{+0.02}_{...}$[c]	0.78 ± 0.08	0.61 ± 0.04	2.64 ± 0.05	-5.25 ± 0.02	2.51/252
EddySed, Grad. *P–T*, (dis)eq. chem., $\mathcal{N}(1.33, 0.03)_{R_p}$	4.0 ± 0.4	790^{+5}_{-10}	3.83 ± 0.04	$1.23^{+0.02}_{...}$[c]	0.75 ± 0.07	0.60 ± 0.04	2.64 ± 0.05	-5.25 ± 0.01	3.06/246
Adopted values	3.75 ± 0.5	800 ± 50	3.7 ± 0.2	1.3 ± 0.15	0.75 ± 0.25	0.55 ± 0.10	$2.6^{+0.2}_{-0.3}$	$-5.2^{+0.1}_{-0.2}$	⋯

Notes. For each type of model considered (evolutionary, self-consistent atmosphere, atmospheric retrieval) we record the mean and 1σ confidence interval for the parameters of interest. $\mathcal{U}(x, y)_P$ denotes a uniform from x to y, and $\mathcal{N}(x, y)_P$ denotes a normally distributed prior with mean x and standard deviation y on the parameter P. There are $233 + 39 + 4\text{-}\Sigma P_i = 276\text{-}\Sigma P_i$ degrees of freedom for each comparison considering all the data visualized in Figure 2, and $233\text{-}\Sigma P_i$ for each comparison considering only the GRAVITY spectrum.

[a] We present $\log(K_{zz})$ for RCE grids that include it as a free parameter, and $P_{\rm quench}$ for `petitRADTRANS` retrievals that implement (dis)equilibrium chemistry.

[b] All model fits use our dynamical mass estimate as a prior influencing $\log(g)$ given R.

[c] Denotes a parameter that has piled up at a prior boundary.

[d] When fitting only the GRAVITY spectrum with linear interpolations of the `Exo-REM` grid, we observed a multimodal posterior; we report the median and CI for the low- and high-temperature modes in two lines in this table.

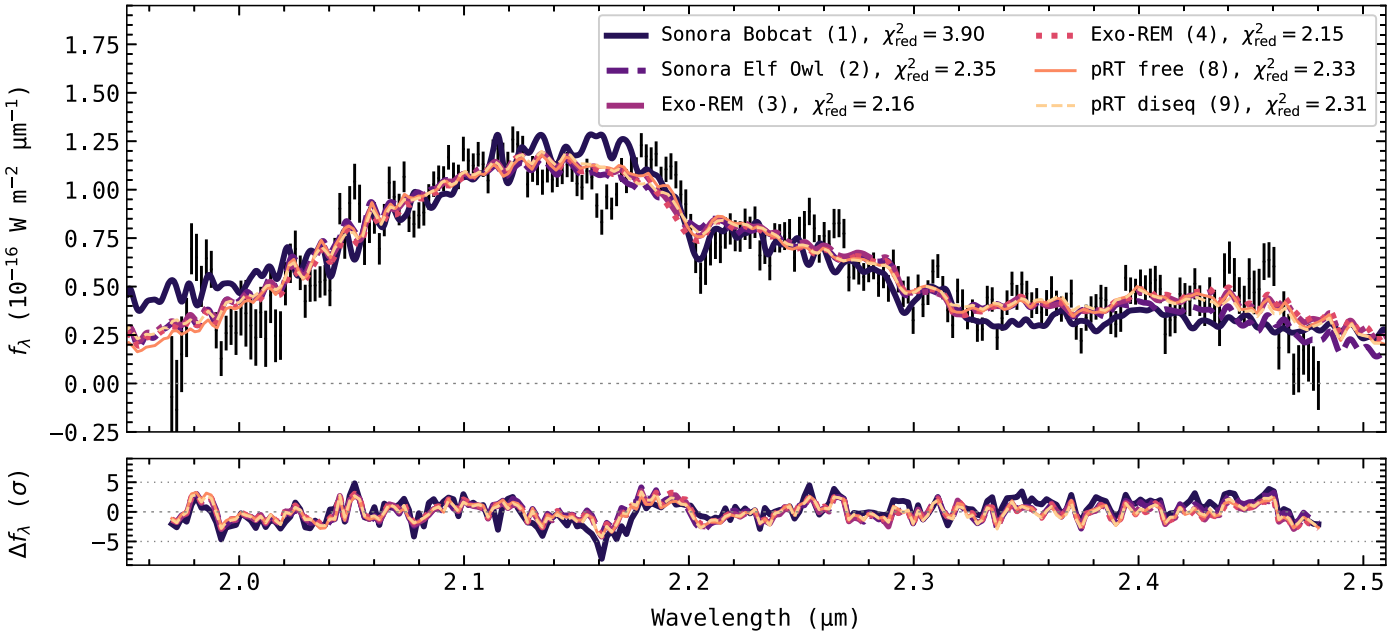

Figure 5. Model comparisons to the GRAVITY spectrum (not including additional data sets). Shown are models, numbered based on their appearance in Table 4, and the reduced χ^2 of the fit. Most models provide a reasonable fit to the spectrum, but only the cloudy `Exo-REM` grid and the cloudy, free chemistry `petitRADTRANS` retrieval result in physically plausible radii ($R > 1.1 R_J$).

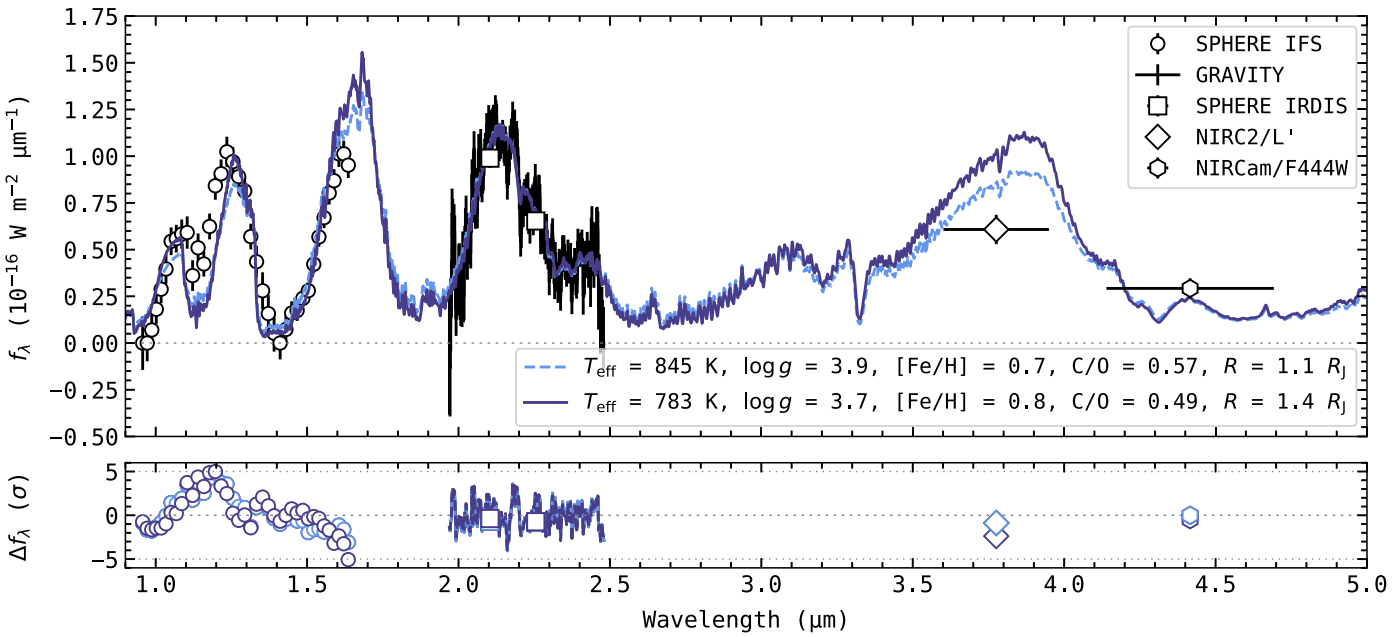

Figure 6. Interpolated `Exo-REM` atmospheric models assuming the dynamical mass as a prior (dashed light blue) and fixing the dynamical mass and evolutionary model prediction for radius (solid dark blue). To better fit the SPHERE H1 band spectrophotometry and the Keck/NIRC2 *L'* photometry, the sampler prefers unphysically small radii (high log(g)), higher effective temperatures, higher C/O, and lower metallicity. The GRAVITY data rule out higher-temperature models, very low and very high C/O ratios, and solar metallicities and are matched well by the model in either case.

posterior distribution of parameters. The drawback to this technique is that these parameterized model atmospheres are not necessarily physically consistent, but the technique allows for the flexible exploration of many parameters of interest.

We used the `petitRADTRANS` radiative transfer package to model the emission spectrum of AF Lep b and to conduct our atmospheric retrievals (P. Mollière et al. 2019, 2020; E. Alei et al. 2022). We refer the reader to P. Mollière et al. (2020), Z. Zhang et al. (2023), and E. Nasedkin et al. (2024b) for full descriptions of the retrieval implementation, particularly the chemistry. We also refer the reader to E. Nasedkin et al. (2024a) for a description of the code and sampler and to M. Nowak et al. (2020), P. Mollière et al. (2020), J. Kammerer et al. (2021), and W. O. Balmer et al. (2023) for previous usage of the retrieval in the context of GRAVITY observations. `species` was used as a wrapper for setting up the model framework and for initializing nested sampling via `pyMultiNest`, now with 2000 live points in constant sampling efficiency mode with an efficiency of 0.05 in order to explore the posterior distributions.

To briefly summarize, these retrievals use the correlated-k treatment for opacities, including line species for H_2O (O. L. Polyansky et al. 2018), CO (L. S. Rothman et al. 2010), CH_4 (S. N. Yurchenko et al. 2017), CO_2 (S. N. Yurchenko et al. 2020), NH_3 (P. A. Coles et al. 2019), HCN (R. J. Barber et al. 2014), H_2S (A. A. A. Azzam et al. 2016), PH_3 (C. Sousa-Silva et al. 2015), FeH (S. Wende et al. 2010), Na (N. F. Allard et al. 2019), K (N. F. Allard et al. 2016), SiO (E. J. Barton et al. 2013), TiO (L. K. McKemmish et al. 2019), and VO (L. K. McKemmish et al. 2016); Rayleigh scattering opacities for H_2 and He (A. Dalgarno & D. A. Williams 1962; Y. M. Chan & A. Dalgarno 1965); and collision-induced absorption of H_2 and He (J. Borysow et al. 1988; A. Borysow et al. 1989, 2001; C. Richard et al. 2012). Many of these opacities are available from the ExoMol database (K. L. Chubb et al. 2021), in the "petitRADTRANS" format.[31]

E. Nasedkin et al. (2023) showed that unaccounted-for correlations in input data for spectral retrievals can strongly bias the resulting atmospheric inferences. As in Section 3.2.2, we estimate the correlated noise in the SPHERE IFS spectrum using a Gaussian process by sampling the parameters of a squared-exponential kernel that estimates the correlation matrix of the spectrum. Again, we provide the retrieval likelihood function of the empirical GRAVITY correlation matrix.

We considered two chemistry parameterizations, both described in E. Nasedkin et al. (2024b). The first is based on an initial assumption of equilibrium chemistry modified by transport-induced quenching. Here metallicity [M/H] and C/O are free parameters and abundances of individual molecules at a given pressure and temperature (set by the retrieved P–T profile) are determined by interpolating along a temperature/pressure/[M/H]/(C/O) table that was computed using `easyCHEM` (P. Mollière et al. 2017). To approximate the effect of transport-induced chemical disequilibrium ("vertical mixing"), a "quench pressure" parameter is sampled. Above this pressure, the abundances of H_2O, CO, and CH_4 are set constant to the value at $P_{\rm quench}$. We refer to this as the (dis)equilibrium chemistry parameterization. The second chemistry parameterization is referred to as "free" chemistry, where the vertically constant abundances for each molecule are sampled as free parameters, with the constraint that the sum of these mass fractions is less than 1.

Three P–T parameterizations were considered, and they are described in E. Nasedkin et al. (2024b). One retrieval relied on a cubic "spline" interpolation profile with an oscillation penalty term (M. R. Line et al. 2015). Another used the "three-part" parameterization introduced in P. Mollière et al. (2020), which samples three free temperature nodes above the photosphere, follows the Eddington profile in the photosphere, and is forced onto a moist adiabat up to the radiative–convective boundary. The majority of the retrieval experiments used the "gradient" parameterization introduced by Z. Zhang et al. (2023), where the gradient of the P–T profile is sampled, instead of the temperature at a given pressure. This parameterization allows for prior constraints on the gradient based on "self-consistent" RCE models. The gradient $d\ln T/d\ln P$ is sampled at six pressure nodes spaced logarithmically between 1000 and 10^{-3} bars, and normally distributed priors are adopted for each node based on the results of a sample of self-consistent RCE models. We adopt the same priors on $d\ln T/d\ln P$ listed in Equation (3) of Z. Zhang et al. (2023) and Table 6 in E. Nasedkin et al. (2024b), derived from the RCE models of M. W. Phillips et al. (2020), M. S. Marley et al. (2021), T. Karalidi et al. (2021), S. Mukherjee et al. (2022), and B. Lacy & A. Burrows (2023).

The majority of our retrievals used the A. S. Ackerman & M. S. Marley (2001) parameterization for clouds (see Section 2.4 in P. Mollière et al. 2020, for the implementation of this cloud model in `petitRADTRANS`), which is referred to as the "EddySed" model here. This model defines a cloud sedimentation efficiency parameter $f_{\rm sed}$ that sets the cloud mass fraction X^c,

$$X^c(P) = X_0^c\left(\frac{P}{P_{\rm base}}\right)^{f_{\rm sed}},$$

where $P_{\rm base}$ is found by intersecting our P–T profile with the saturation vapor pressure profile of a given cloud species. X_0^c, the value of X^c at $P_{\rm base}$, is allowed to vary in terms of $X_{\rm eq}^c$, the cloud mass fraction assuming equilibrium condensation at $P_{\rm base}$. The cloud particle vertical eddy diffusion coefficient K_{zz} is also allowed to vary, which effectively sets an average particle size given $f_{\rm sed}$. The width of a lognormal particle size distribution σ_g about this average particle size is another free parameter. We included opacity contributions from iron (Fe; T. Henning & R. Stognienko 1996), enstatite ($MgSiO_3$; A. Scott & W. W. Duley 1996; C. Jaeger et al. 1998), and potassium chloride (KCl; E. J. Barton et al. 2014) grains. The crystalline (DHS irregular) opacities were adopted because the observations do not reach long-enough wavelengths to distinguish between amorphous and crystalline grains for any of the species considered. These are calculated using OpacityTool (M. Min et al. 2005), which makes use of software from O. B. Toon & T. P. Ackerman (1981). The wavelength-dependent opacities are added to the wavelength bins, as they vary slowly compared to the line opacities.

The fully parametric cloud model, introduced as "cloud model 2" in P. Mollière et al. (2020), that we dub the "agnostic" cloud model was used when conducting retrievals on only the GRAVITY spectrum, since the clouds considered here are "gray," that is, wavelength independent across the K band. This model has

$$\kappa_{\rm tot} = \kappa(P)\left(\frac{\lambda}{\lambda_R}\right)^{\xi}, \tag{4}$$

where $\kappa_{\rm tot}$ is the total cloud opacity (both scattering and absorbing components), $\kappa(P)$ is the value at 1 μm at pressure P, λ_R is a reference wavelength, and ξ is the spectral slope of the cloud. Then, we define the wavelength-dependent opacity of the cloud, $\kappa_{\rm cloud}(\lambda,P)$, as

$$\kappa_{\rm cloud}(\lambda, P) = \kappa_0\left(\frac{P}{P_{\rm base}}\right)^{f_{\rm sed}}, \tag{5}$$

where $P < P_{\rm base}$ and κ_0 and $f_{\rm sed}$ are free parameters describing the cloud base pressure in units of bars and the cloud opacity in units of $\rm cm^2\ g^{-1}$ at the reference wavelength, respectively, and the cloud scale height dies off. We also parameterize a single

[31] www.exomol.com

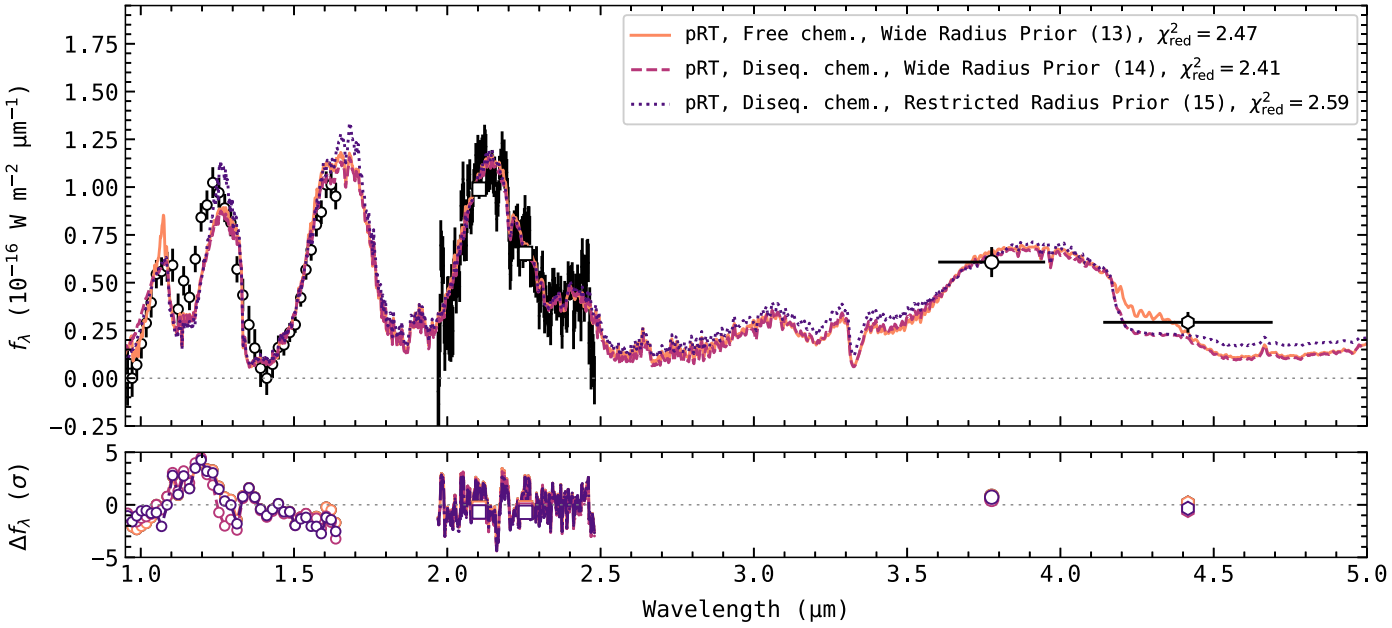

Figure 7. `petitRADTRANS` retrieval examples, as described in Section 3.2.3. These three models use the EddySed cloud model with Fe, $MgSiO_3$, and KCl clouds and the RCE-prior-constrained gradient P–T profile. The solid orange line represents a retrieval run with free chemistry and a wide ($0.5R_J$–$2.0R_J$) uniform prior on radius; the dashed magenta line, a run with (dis)equilibrium chemistry and the same wide uniform radius prior; the dotted dark-purple line, a run with (dis)equilibrium chemistry and a restricted ($1.2R_J$–$1.5R_J$) uniform radius prior following Z. Zhang et al. (2023). Each retrieval is labeled with its reduced χ^2; their associated parameters appear in Table 4, lines 13–15.

scattering albedo ω such that

$$\kappa_{abs} = (1 - \omega)\kappa_{tot}. \quad (6)$$

This model was also briefly compared against the full data set, coupled with the gradient P–T profile, but was not preferred when compared to the EddySed model.

We constructed a series of retrieval tests driven by outstanding questions raised in Z. Zhang et al. (2023) and P. Palma-Bifani et al. (2024); these are recorded in Table 4 and discussed in Section 4. These experiments were designed to answer the following questions: (1) How does the new GRAVITY spectrum change, revise, or confound the results of previous studies? (2) What do the composition inferences suggest about the planet's properties and formation history? (3) What data and model deficiencies are present? (4) What information is expressed in the GRAVITY K-band spectrum of an "AF Lep b-like" planet, that is, what can one learn from retrievals conducted on the GRAVITY spectrum alone? The results are discussed in Sections 4.4–4.5 regarding points 1–3 and in Section 4.6 regarding point 4. The "GRAVITY-only" retrievals are included in Figure 5, a subset of the full SED retrievals is visualized in Figure 7, and their corresponding P–T profiles are shown in Figure 8. No retrieval resulted in a derived radius that was consistent with evolutionary model expectations within uncertainties, aside from the free chemistry "GRAVITY-only" retrieval, which has a large uncertainty ($R = 1.22^{+0.19}_{-0.14}\,R_J$) and fails to predict the observed Y and J bands.

4. Discussion

4.1. The Orbit of AF Lep b: Formation, System Architecture, and Debris Disk Stirring

Recent population-level studies of directly imaged planets indicate that "planetary-mass" ($\lesssim 13 M_{Jup}$) companions exhibit on average lower eccentricity than brown dwarfs (B. P. Bowler et al. 2020; C. R. Do Ó et al. 2023; V. Nagpal et al. 2023), although a larger sample and longer orbital coverage are likely needed to confirm this (see discussion in C. R. Do Ó et al. 2023). RV surveys, with a larger sample size skewed toward significantly shorter periods than directly imaged companions, show that the eccentricity distribution of single gas giants appears to pile up at circular orbits with a long tail out to $e \sim 0.8$ (L. J. Rosenthal et al. 2024). Both of these results suggest that formation within a gas disk, where drag forces can damp initial eccentricity, result in populations of planets with low eccentricity. Our updated eccentricity measurement, an upper limit of $e < 0.02$, 0.07, and 0.13 at 1σ, 2σ, and 3σ, respectively, is therefore consistent with expectations based on formation within a protoplanetary disk. Our updated inclination angle measurement, $i_{orbit} = 57.°5^{+0.°6}_{-0.°7}$, is consistent with the stellar inclination angle $i_\star = 54°^{+11°}_{-9°}$ (K. Franson et al. 2023b) and therefore with a system in spin–orbit alignment.[32] Spin–orbit alignment, like circular orbits, is preferentially set by formation within the protoplanetary disk, and there is growing evidence for spin–orbit alignment of directly imaged planets when compared against brown dwarf companions (B. P. Bowler et al. 2023; A. G. Sepulveda et al. 2024).

The precisely constrained semimajor axis of the planet, $a = 8.98^{+0.15}_{-0.08}$ au, is also coincident with the peak of the recently observed RV giant planet occurrence rate maximum (B. J. Fulton et al. 2021; A. M. Lagrange et al. 2023), which has been explained by invoking preferential formation of giant planets near their parent protoplanetary disk's ice lines.

The dynamical mass measurement, $M_b = 3.75 M_J \pm 0.5 M_J$, is consistent with that found by previous studies, and the differences in central value are attributable to the correlation between the dynamical mass on the eccentricity (see

[32] Because the stellar polar position angle is unknown, this apparent agreement only represents a lower limit on the true obliquity angle (B. P. Bowler et al. 2023, Section 2).

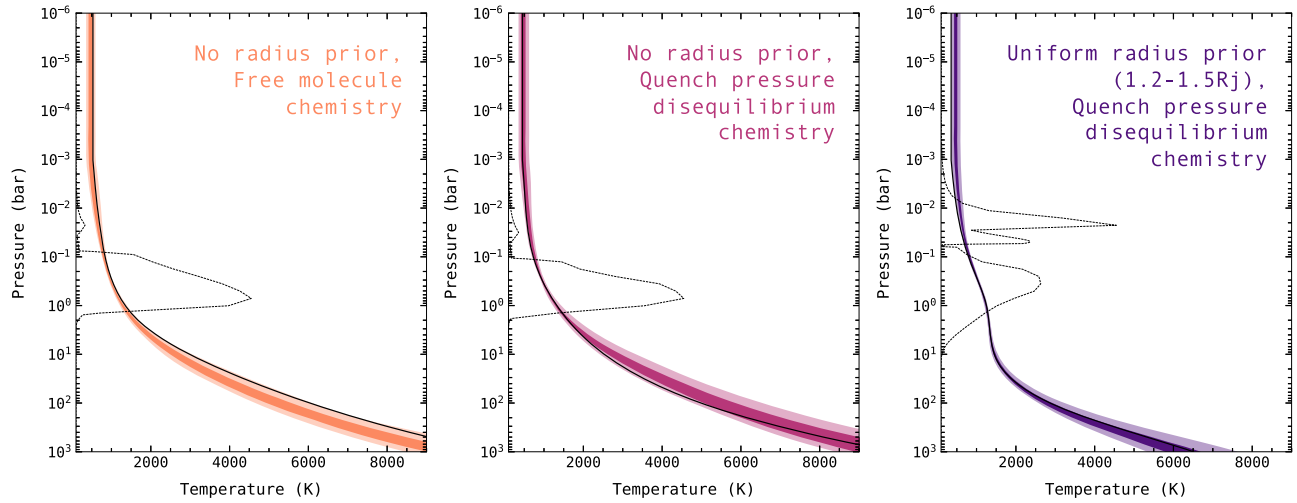

Figure 8. *P–T* profiles corresponding to the retrievals shown in Figure 7. When the sampler is forced to accept solutions with $R > 1.2R_J$, the *P–T* profile is forced away from RCE and into an isothermal shape. This could be indicative of missing cloud/haze opacity due to the parameterization of cloud particle sizes, as discussed in Section 4.4.

Figures 3(e) and (f)). The value is just shy of the $\sim 4M_J$ population split indicated by RV surveys (N. C. Santos et al. 2017; K. C. Schlaufman 2018), which has been suggested to be due to different formation for objects above (gravitation instability) and below (core accretion) the boundary. This precise and now systematically robust dynamical mass estimate also enables the placement of AF Lep b in the planetary mass–metallicity relationship, as discussed below, and provides a useful prior on the surface gravity of the planet for the atmospheric analysis.

This updated orbit also constrains the degree to which AF Lep b can excite (or "stir") planetesimals in the system, enhancing the dust production in the unresolved debris belt. The planet's discovery already ruled out the planet's ability to directly "sculpt" the debris disk (K. Franson et al. 2023b). The stirring argument is interesting insofar as recent theoretical work has cast doubt on the ability of debris disks to "self-stir," indicating that excitation via secular processes from planets might be required to reproduce the population of observed debris disks (A. V. Krivov & M. Booth 2018; T. D. Pearce et al. 2022). Following K. Franson et al. (2023b), by inverting Equation (15) from A. J. Mustill & M. C. Wyatt (2009), we can estimate the minimum mass necessary for a planet on AF Lep b's orbit to stir the exterior debris disk. A. J. Mustill & M. C. Wyatt (2009) give

$$\frac{m_{\rm pl}}{M_\odot} = 1.53 \times 10^3 \left(\frac{1\ {\rm yr}}{t_{\rm cross}}\right) \frac{(1-e_{\rm pl})^{(3/2)}}{e_{\rm pl}} \left(\frac{a_{\rm disk}}{10\ {\rm au}}\right)^{(9/2)} \times \left(\frac{a_{\rm pl}}{1\ {\rm au}}\right) \left(\frac{m_\star}{M_\odot}\right)^{(1/2)}. \quad (7)$$

If we then take $t_{\rm cross}$ as the age of the system, $a_{\rm disk} = 46 \pm 9$ au (T. D. Pearce et al. 2022), and then adopt our posterior distribution on the orbital parameters, we can solve for $m_{\rm pl}$ and compare this to the dynamical mass constraint from the same orbit. The maximum a posteriori orbit (with $e = 0.02$, $a = 8.98$ au, $m_\star = 1.22\,M_\odot$) yields a minimum mass for stirring, given $t_{\rm cross} = 24$ Myr, of $m_{\rm pl} = 4.9 M_J$ (or, for $t_{\rm cross} = 16.3$ Myr, $m_{\rm pl} = 7.2 M_J$). Compared to the dynamical mass of $M_b = 3.75 M_J$., the minimum mass is larger. Hence, our most probable orbit is inconsistent with generating the dust in the system, which would require additional sculpting or stirring planets farther out to explain. Given the deep imaging limits from JWST/NIRCam (K. Franson et al. 2024), such a planet would be of sub-Saturn mass. Considering the entire posterior distribution of orbits, we randomly sample from a normal distribution of $a_{\rm disk}$ and $t_{\rm cross}$ and calculate the fraction of the posterior orbits that are consistent or inconsistent with stirring the disk. We performed this calculation 5000 times for both the isochronal system age 24 ± 3 Myr (C. P. M. Bell et al. 2015) and the kinematic traceback age 16.3 ± 3.4 Myr (J. Lee & I. Song 2024). The result (Figure 9) was that 32% of the orbits are consistent with stirring a planetesimal population at 46 ± 9 au if $t_{\rm cross} = 24 \pm 3$ Myr and that 23% are consistent with stirring that same population if $t_{\rm cross} = 16.3 \pm 3.4$ Myr. Largely, these are orbits in the tails of the posterior, with small but nonzero eccentricities.

AF Lep b, with a nearly circular eccentricity but a relatively large mass, could be the sole planet responsible for "stirring" the system's debris. This seems a simple, plausible explanation given the data. However, given that 2/3 of the posterior is inconsistent with stirring, an equally plausible explanation is that smaller, undetected planets (like sub-Neptunes or super-Earths) at wider separations are shepherding the debris more directly, analogous to Jupiter's and Neptune's influence on the Kuiper Belt. In the near future, continued monitoring of the system at high precision can strengthen this constraint regardless of the systematic uncertainty on the system age. Constraints on the distribution of the debris could be gained by observations with the Atacama Large Millimeter/submillimeter Array or JWST/MIRI. It will be interesting to understand going forward whether other, less massive bodies (which would be consistent with the nondetection from JWST/NIRCam) are needed to shape the debris in the system.

4.2. "The Radius Problem"

At a population level, a "small-radius problem" arises for field (mature, ages >1 Gyr) brown dwarfs at the L/T (and T/Y) transitions, where atmospheric models struggle to reproduce radii estimated using evolutionary tracks, when both classes of tools are fit to match near-infrared observations (see Figure 24 in A. Sanghi et al. 2023). The small-radius problem remains a

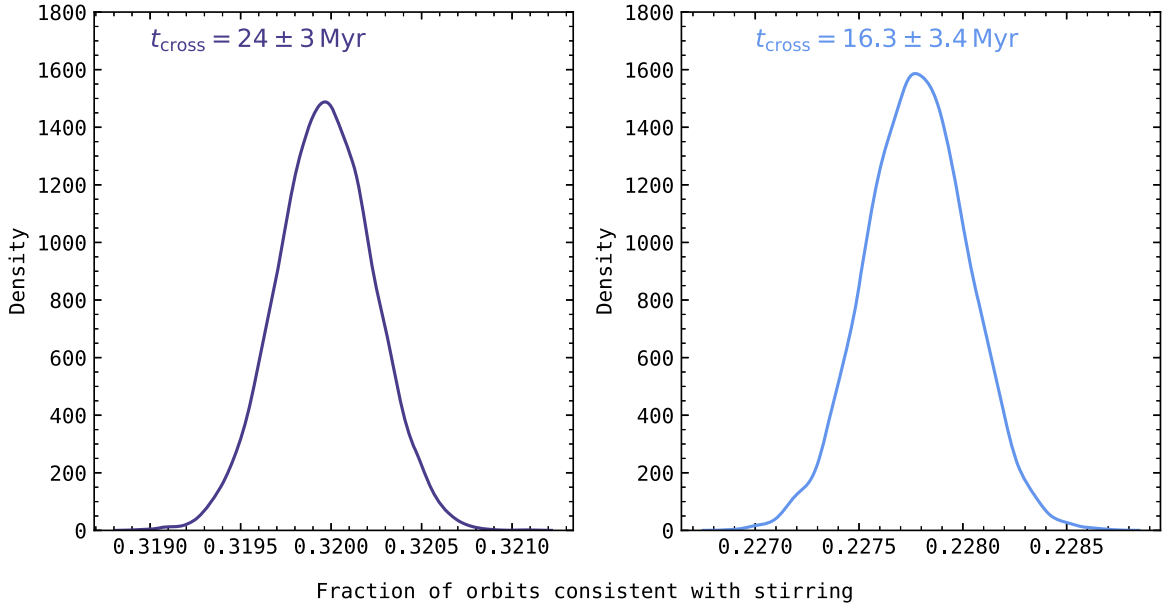

Figure 9. Fraction of AF Lep b orbits consistent with stirring AF Lep's debris disk at 46 ± 9 au (following A. J. Mustill & M. C. Wyatt 2009; T. D. Pearce et al. 2022) for the isochronal age (left; C. P. M. Bell et al. 2015) and the kinematic traceback age (right; J. Lee & I. Song 2024).

persistent issue for retrievals, even when the dynamical mass is known, or mid-infrared observations are available, or high-resolution observations are available (B. Burningham et al. 2017; J. A. Zalesky et al. 2019; E. C. Gonzales et al. 2020; D. Kitzmann et al. 2020; B. Burningham et al. 2021; Z. Zhang et al. 2021a, 2021b; E. C. Gonzales et al. 2022; A. Lueber et al. 2022; J. W. Xuan et al. 2022; W. O. Balmer et al. 2023; K. Franson et al. 2023a; C. E. Hood et al. 2023; J. M. Vos et al. 2023; J. W. Xuan et al. 2024a). There is also an equivalent but opposite issue, a "large-radius problem," for hotter M-type objects: evolutionary models predict smaller radii and colder temperatures than are measured spectroscopically. In W. O. Balmer et al. (2024), we found agreement at the 1σ–2σ level when forward modeling a young, low-mass "benchmark" M-type companion, highlighting the variance of this problem: individual targets and observations may be more or less affected by this problem depending on a number of factors, like spectral type, data coverage, resolution, or model choice. Both small- and large-radius problems affect retrieval studies and forward modeling studies (e.g., J. W. Xuan et al. 2024b, in the case of retrievals on M-dwarf companions). This issue is understood to be an atmospheric model deficiency, rather than an evolutionary model deficiency, since it would be physically impossible for an object of order $10^0 M_J$–$10^2 M_J$ in mass to have a radius of $\lesssim 0.8 R_J$ given the H–He equation of state (G. Chabrier & A. Y. Potekhin 1998; G. Chabrier et al. 2019; G. Chabrier & F. Debras 2021; G. Chabrier et al. 2023).

Intrinsically younger or lower-mass objects will have lower surface gravities than the older field population of brown dwarfs (e.g., J. K. Faherty et al. 2016; M. C. Liu et al. 2016), and since clouds become more prominent at lower surface gravity, these objects tend to have redder colors, cooler effective temperatures, and higher variability amplitudes (e.g., M. C. Liu et al. 2016; J. M. Vos et al. 2022). The interplay between age, mass, and composition makes the atmospheric modeling of these objects particularly challenging. For example, the spectrophotometry of the HR 8799 planets (C. Marois et al. 2008, 2010), being much fainter and with much redder colors than their field spectral counterparts, has been challenging to model with physical consistency (see E. Nasedkin et al. 2024b, for updated GRAVITY spectroscopy of these planets and an exhaustive retrieval analysis). At their discovery, the fidelity of the cloud model was seen to have an impact on the plausibility of the determined radii for these planets (C. Marois et al. 2008, supplementary materials). Many early analyses of HR 8799 and other substellar objects found too small radii (e.g., B. P. Bowler et al. 2010; T. S. Barman et al. 2011a, 2011b; M. S. Marley et al. 2012). For the young late L-type brown dwarf companion 2M1207b, this radius problem was rectified by increasing the complexity of the models: including cloud opacity with intermediate particle sizes and disequilibrium chemistry (T. S. Barman et al. 2011b; A. J. Skemer et al. 2011).

For the remainder of this discussion, we make the distinction between "physically implausible" radii and "inconsistent" radii. The former is a model-estimated radius too small to realistically satisfy the substellar object's equation of state and thus the predictions from evolutionary models for any age. The latter is an atmospheric-model-estimated radius that is not consistent with the ones obtained with evolutionary tracks but physically plausible. In this case discrepancies could arise from insufficient model physics in either class of model, or inaccuracies in the measurements of age, dynamical mass, etc., for the planet. Since this section focuses on the atmospheric modeling for AF Lep b, we mostly discuss possible limitations of atmospheric models. We recognize, however, that missing information in evolutionary tracks might also contribute to "inconsistent" radii.

4.3. Previous Models of the Planet's Atmosphere

In the case of AF Lep b, discovery studies found that it straddled the low-gravity L/T transition but individually did not have enough data to model the planet's atmosphere in much detail (R. J. De Rosa et al. 2023; K. Franson et al. 2023b; D. Mesa et al. 2023). Two subsequent studies collated the discovery observations and modeled this ensemble with `petitRADTRANS` retrievals (Z. Zhang et al. 2023) and with

the Exo-REM forward models (P. Palma-Bifani et al. 2024), and both encountered the small-radius problem. Z. Zhang et al. (2023), by imposing a prior on the shape of the *P–T* profile based on the results of RCE forward models (their gradient *P–T* parameterization, described in Section 3.2.3), could effectively force the retrieved EddySed model to produce cloudy atmospheres. This is an elegant solution to the degeneracy between *P–T* flexibility and cloud opacity in retrievals, but it did not appear to resolve the small-radius problem (as our results also demonstrate). In an attempt to address the small-radius problem, Z. Zhang et al. (2023) imposed a prior on the radius based on evolutionary model predictions, restricting the allowed radii to values $R \in \mathcal{U}(1.2, 1.5)$, as opposed to the uninformative prior commonly adopted when performing retrievals $R \in \mathcal{U}(0.5, 2.0)$. P. Palma-Bifani et al. (2024) instead impose a prior on the surface gravity explicitly, $\log(g) \sim \mathcal{N}(3.7, 0.1)$, combining predictions from a single set of evolutionary models (G.-D. Marleau et al. 2019) and the dynamical mass estimate from Z. Zhang et al. (2023). The detection of the planet at 4.4 μm from JWST/NIRCam (K. Franson et al. 2024) enabled an updated retrieval analysis using the same framework as in Z. Zhang et al. (2023). As their Figure 3 indicates, the relatively low 4.4 μm flux of the planet is due to out-of-equilibrium CO absorption; their retrievals find deep quenching pressures (running up against their prior boundary of 3, peaking near 2.80 bars), high metallicities ([Fe/H] $= 1.67 \pm 0.20$), and supersolar C/O (C/O $= 0.65 \pm 0.05$).

While AF Lep b lies in a temperature–gravity regime that is plagued by the small-radius problem, both prior-based solutions appeared to resolve the issue. Armed with our new GRAVITY spectrum that sets a stronger temperature–pressure constraint owing to the unambiguous methane absorption, we sought to revisit these results.

4.4. Modeling the Atmosphere of AF Lep b

4.4.1. Forward Model Results

We began our atmospheric analysis comparing forward models to only the GRAVITY spectrum (see Figure 5). The cloudless, chemical equilibrium Sonora Bobcat models provided a relatively poor fit to the data ($\chi^2_{\rm red} \sim 4$; see Table 4) and physically implausible radii. The cloudless, chemical disequilibrium Sonora Elf Owl models provided a better fit ($\chi^2_{\rm red} \sim 2.2$) and indicate strong vertical mixing ($\log(K_{zz}) = 7.7$) in broad agreement with the findings of K. Franson et al. (2024) but still resulted in physically implausible radii. The cloudy, chemical disequilibrium Exo-REM models fit the GRAVITY spectrum well and resulted in a (multimodal) posterior, where half of the posterior samples (in one mode) encompassed physically plausible radii and another half (in the other mode) were physically implausible.

We then compared the entire SED of AF Lep b to the cloudy, solar-metallicity, chemical equilibrium BT-Settl models, which provided a very poor fit to the data ($\chi^2_{\rm red} \sim 6$). This was to be expected, as both the model fits to the GRAVITY spectrum alone and previous studies (Z. Zhang et al. 2023; K. Franson et al. 2024) indicate that an enhanced metallicity and chemical disequilibrium are required to explain the planet's spectrum. We then compared the full data set to the Exo-REM models, first without restrictions on the radius/surface gravity and then by effectively fixing the surface gravity to the expectations from evolutionary models, given our dynamical mass estimate. For the first case we find $T_{\rm eff} \sim 850$ K, an enriched metallicity [M/H] $= 0.69 \pm 0.02$, and C/O $= 0.57 \pm 0.01$. The log(g) is higher than expected given the evolutionary models, and the mass is driven $\sim 0.5 M_{\rm J}$ higher than the prior, resulting in a radius that is physically plausible but inconsistent at $>5\sigma$ from the expectations from evolutionary models ($R_{\rm Exo-REM} = 1.14 R_{\rm J} \pm 0.02 R_{\rm J}$, compared to $R_{\rm SM08} = 1.30 R_{\rm J} \pm 0.01 R_{\rm J}$). This in turn leads to a higher effective temperature estimate than predicted by evolutionary models. In the second case, we fixed the mass to our dynamical mass central value and the surface gravity to 3.7, which results in an $R = 1.35 R_{\rm J}$, provided that the parallax is not driven away from its prior value. The parallax prior on the system from Gaia is strong enough to hold, and we recover this physically plausible and consistent-with-evolutionary-tracks radius in this case. Here we find a lower effective temperature in line with evolutionary model predictions $T_{\rm eff} \sim 780$ K, a more enriched metallicity [M/H] $= 0.77 \pm 0.03$, and a slightly subsolar C/O $= 0.49 \pm 0.01$. The difference in reduced goodness of fit between these models is $\Delta\chi^2_{\rm red} = -0.2$, slightly favoring the inconsistent model (as the analysis in P. Palma-Bifani et al. 2024 and Figure 6 shows, it appears that this is primarily driven by the slope of the SPHERE spectrum and the magnitude of the Keck/NIRC2 *L'* photometry).

With Exo-REM, all the estimated radii are physically plausible, but it was not feasible to use our grid sampling scheme to recover consistent radii without fixing the surface gravity and mass a priori (as in the second case). For instance, we attempted to place the prior $\log(g) \sim \mathcal{N}(3.7, 0.1)$ as in P. Palma-Bifani et al. (2024), which is less informative than simply fixing the value to 3.7 and more accurately captures our uncertainty on the system (and planet) age, initial conditions, etc., but the posterior distributions for these tests were always driven away from this prior range and to the equivalent of the posterior from the first case. Still, it is encouraging that the Exo-REM model comparisons resulted in derived radii that were larger than $1.0 R_{\rm J}$. An improvement could be gained by varying the choice of the supersaturation parameter in the models, a ratio that, like $f_{\rm sed}$ in the EddySed model, informs the cloud thickness. In the models we used, the supersaturation parameter is fixed to an intermediate value of $S = 0.03$, but its exact value shapes the *Y* and *J* bands and could reasonably vary anywhere between 0.001 and 0.1, based on the range of water nucleation in Earth's atmosphere (see Figure 11 in B. Charnay et al. 2018). The public grid also does not include any sulfide salt clouds (like KCl) that may contribute additional wavelength-dependent opacity to this region. Finally, the uncertainties we measure based on our method of grid comparison could benefit from the use of a spectral emulator, where, instead of multilinearly interpolating across spectra, the grid of precomputed spectra is transformed via principle component analysis into eigenspectra, and the likelihood function can be modified to include the uncertainty due to the interpolation (I. Czekala et al. 2015; Z. Zhang et al. 2021a, 2021b). This results in more reasonable uncertainty estimates with wider posterior distributions on the sampled parameters and might not require that we fix key parameters a priori to recover physically consistent results.

4.4.2. Retrieval Results

We constructed our retrieval experiments to incrementally increase the complexity of the cloud prescription (or *P–T*

profile) and then add plausible physically motivated priors (like the RCE or radius priors from Z. Zhang et al. 2023), in order to better understand the structure of the planet's atmosphere and address or understand limitations of our models (primarily, the small-radius problem). First, inspired by the suggestion in P. Tremblin et al. (2015), we fit the data with a cloudless retrieval using the fully flexible cubic spline *P–T* profile and the (dis)equilibrium chemistry parameterization. This fit converged to an unphysical radius ($R = 0.70R_J \pm 0.05R_J$) with an isothermal photosphere. As in Z. Zhang et al. (2023) and K. Franson et al. (2024), we retrieved a deep quenching pressure $P_{\rm quench} = 2.67 \pm 0.06$ bars, indicating that vertical mixing was transporting hot, out-of-equilibrium gas from deep in the planet's atmosphere into the photosphere, but, unlike those results, we find a more moderately enriched metallicity of $[{\rm Fe/H}] = 0.83 \pm 0.08$. As we changed the retrieval framework, the resulting small-radius problem persisted, and in general the qualitative results remained the same: a moderately enriched metallicity, C/O near solar or slightly higher, and a deep quench pressure.

We then fit the data with the single agnostic cloud model, the gradient *P–T* profile, and free chemistry again with a wide radius prior: while the *P–T* profile was influenced by the RCE priors, this also converged to an unphysical radius with an isothermal photosphere, which prompted us to add multiple cloud layers of varying specie using the EddySed model. We included three cloud species (Fe, $MgSiO_3$, and KCl), starting with the flexible three-part *P–T* profile, (dis)equilibrium chemistry, and a wide radius prior: this again converged to a physically implausible radius with an isothermal photosphere and relatively unconstrained cloud properties—notably, the quench pressure for this retrieval was slightly lower than the other values but more uncertain, $P_{\rm quench} = 2.28 \pm 0.22$ bars.

We added the extra constraint of the gradient *P–T* profile parameterization with RCE-based priors. These retrievals resulted in consistently cloudy atmospheres with more adiabatic *P–T* profiles, with a strong contribution from $MgSiO_3$ (as in Z. Zhang et al. 2023; K. Franson et al. 2024). We compared free versus disequilibrium chemistry using this gradient *P–T* parameterization, and while the fit to the (dis) equilibrium chemistry was marginally better ($\Delta\chi^2_{\rm red} = 0.06$), the small-radius problem persisted.

We moved on to using Z. Zhang et al.'s (2023) evolutionary-model-informed uniform radius prior, $R \in \mathcal{U}(1.2, 1.5)$, with the gradient *P–T*, (dis)equilibrium chemistry, and EddySed clouds: effectively this retrieval reproduced the setup in Z. Zhang et al. (2023) and K. Franson et al. (2024), except that we include our new data and include GP parameters to estimate the correlation in the SPHERE spectrum. The posterior piled up against the lower bound of the radius prior range and the *P–T* structure of the photosphere was driven from the RCE priors toward a more isothermal shape, even when we placed a normally distributed prior on the radius based on the evolutionary models. This indicated to us that the EddySed model as currently implemented in `petitRADTRANS` is unequipped to explain our observations with physical consistency (see Section 4.4).

4.4.3. Small Inferred Radii and Cloud Particle Sizes

We constructed our retrieval experiments to incrementally increase the model cloud treatment's complexity and then add plausible, physically motivated priors, but all the retrievals we attempted yield physically implausible radii or posteriors that pile up onto the lower bound of the prior space. Overall, the GRAVITY spectrum appears to set a stronger constraint on the correlated atmospheric parameters $T_{\rm eff}$ and $\log(g)$ than previously available *K*-band photometry. In this context, we can see that the restrictive radius prior from Z. Zhang et al. (2023) was effectively a soft $T_{\rm eff}$, $\log(g)$ prior; previously available observations did not have sufficient statistical leverage to push the retrieval away from reproducing the prior. Our high-quality GRAVITY data do, resulting in solutions that exhibit a physically implausible small radius again, even when a normally distributed prior is placed on the expected radius.

It could be that in the case of AF Lep b the root cause of the "small-radius problem" lies in the lack of diversity of cloud prescription across our models (see Section 3.2.3). We have a few tentative lines of evidence to support this. In W. O. Balmer et al. (2023) we found that with the EddySed cloud model within our `petitRADTRANS` retrievals we were unable to reproduce the expected solar metallicity of a massive brown dwarf companion (even when enforcing cloud opacity in the photosphere, albeit with a different prescription than the gradient *P–T* profile used here). In this case, the spectrum was well fit with the solar-metallicity, chemical equilibrium `BT-Settl` grid that implements microphysics-motivated cloud particle size distributions. As discussed in that work, the retrieval overcompensates for the cloud model's inability to capture both the shape of the *Y* and *J* bands (the wavelength-dependent slope) and the overall opacity required to fit the near-IR (the optical depth) simultaneously. Instead, the retrieval found some values for the EddySed cloud that reproduce the optical depth and then increased the opacity in the *Y* and *J* bands by raising the atmospheric metallicity. This indicates to us that the parameterization of the clouds may be too rigid in some aspects but not flexible enough in other aspects to produce models with physical consistency. Additionally, the `Exo-REM` models do yield the best fits to our data with physically plausible (if not fully consistent) radii. This grid also implements microphysics-motivated cloud particle size distributions, which might be the reason underlying this better agreement. The particle sizes set by microphysical arguments typically have more small grains deeper in the atmosphere than the EddySed model, as we discuss below.

Recent papers have shown that the particle size distributions for the clouds in low-gravity substellar objects diverge strongly from those given by the EddySed model prescription. This can be seen in Figure 2 from C. Helling et al. (2008), or by comparing, for instance, Figure 6 in A. S. Ackerman & M. S. Marley (2001) and Figure 7 in D. Samra et al. (2022). More specifically, D. Samra et al. (2022) show that fragmentation becomes a dominant process in shaping the cloud particle size distribution in low surface gravity atmospheres, as collisions are driven by atmospheric turbulence. J. L. Luna & C. V. Morley (2021) show that the mid-infrared silicate absorption feature observed in field brown dwarf spectra can be best fit using two populations of small grains, rather than the EddySed prescription where the size of the grain-given pressure decreases monotonically. We might expect that the deep quench pressure (strong vertical mixing) implied by our GRAVITY spectrum and the JWST photometry for AF Lep b contributes to enhanced particle–particle collisions within the atmosphere, especially given the planet's relatively low temperature and surface gravity. This would result in a run of mean particle size versus pressure that is much

steeper (e.g., smaller particles throughout the photosphere down to the cloud deck) and varies nonlinearly. The assumption of a lognormal particle size distribution could therefore be one of the limiting factors in our cloud parameterization (in particular, see Figure 8 in P. Gao et al. 2021, comparing particle size distributions from the CARMA framework, and see the discussion in the paragraph below regarding hazes, which might motivate more larger particles higher up in addition to the smaller particles throughout the photosphere). Future work could look to incorporate the results of these theoretical studies into parametric retrievals, perhaps with interpolations across tables of precomputed cloud properties derived from microphysical models, or with differently parameterized particle size distributions, or as priors on retrieved vertically varying parameters.

Along these lines, it could be that the lower-than-expected radii indicate an inhomogeneous photosphere, for instance, patchy clouds with varying degrees of coverage. This has been suggested as a potential improvement for retrievals suffering from the small-radius problem (e.g., Section 6.2 in B. Burningham et al. 2021), but even in retrievals where a simple cloud coverage parameter is constrained and preferred over a purely homogeneous model, the small-radius problem persists (J. M. Vos et al. 2022).

In addition, as noted by B. Burningham et al. (2021), if the small radius indicates dark patches on an inhomogeneous atmosphere, they must be clouds of significantly different properties from those we retrieve based on our photospheric constraints, having different particle size distributions and/or different compositions, perhaps very large fluffy particles high up to maintain a gray opacity that can suppress a significant fraction of the planet's flux. We note here that such an opacity source is rather suggestive of a high-altitude haze or, more generally, of aggregate cloud particles in the upper atmospheric layers (for a recent review, see S. Vahidinia et al. 2024). AF Lep b, being relatively close to its host, could experience a significant UV flux that could drive haze production, similar to those observed on Jupiter (X. Zhang et al. 2013).

4.4.4. Adopted Atmospheric Parameters: Strong Evidence for Moderate Metallicities

We see, as does other contemporary retrieval work (J. W. Xuan et al. 2024a), that the small-radius problem does not necessarily invalidate the atmospheric abundances we derive, although their interpretation requires caution. Indeed, fixing the radius (when comparing the `Exo-REM` forward models) results in a difference of 0.08 in C/O and 0.08 dex in [Fe/H] between the best-fitting fixed radius and free radius cases. The range of [Fe/H] across our three-cloud, gradient *P–T* profile `petitRADTRANS` retrievals from the wide radius case to the restricted radius and normal prior radius case is negligible within the statistical uncertainties, and C/O varies by 0.1 with statistical uncertainties of 0.05. The similarity in the range of abundances between our forward model fits and retrievals also lends some credence to the values themselves. While it would be foolhardy to adopt one of the results and its statistical uncertainties as the "true" value, we can reasonably adopt a range of values averaged over our model exploration and compare this to previous results and formation model expectations.

Across our retrievals, we find in general an enriched metallicity ([Fe/H], $\mu_{1/2} \in [0.3\text{–}0.9]$, $\mu_{1\,\sigma} \sim \pm 0.07$]) that is in agreement with P. Palma-Bifani et al. (2024) and our `Exo-REM` forward model best fits. Our revised metallicity disagrees with the very enriched values found by previous `petitRADTRANS` retrievals ([Fe/H] $= 1.67^{+0.17}_{-0.21}$; Z. Zhang et al. 2023; K. Franson et al. 2024). These previous results were obtained with a low-resolution spectroscopy up to 1.6 μm and photometry redward, in *K* band, *L'* band, and then F444W. Clouds were enforced using the prior restricted gradient *P–T* parameterization and physically motivated uniform radius priors (similar to the last line of Table 4). This very enriched value appeared to be in tension at $\sim 1\sigma$ with the planetary mass–metallicity relationship (D. P. Thorngren et al. 2016, and see Section 4.5, Figure 10). By directly constraining the methane abundance with the GRAVITY spectrum and more strongly constraining the cloud wavelength slope with the updated SPHERE spectrum, our observations have elucidated this tension. One way the retrievals can suppress the flux of the atmosphere to match the data is by turning up the metallicity. Without strong constraints on the cloud properties, or a high-enough signal methane constraint, but with a restriction to consistent radii (as discussed above), the previous retrievals appear to have accepted solutions where the metallicity is exceptionally enhanced. In this paper, regardless of the radius prior, our data sets a strong enough constraint to systematically revise the metallicity toward more moderately enriched values (but still statistically significantly enriched compare to the stellar value; see Section 4.5). Our revised metallicity agrees exceptionally well with the planetary mass–metallicity trend.

We find C/O ratios that range about the solar value ($\mu_{1/2} \in [0.43\text{–}0.61]$, $\mu_{1\,\sigma} \sim \pm 0.05$). We find effective temperatures ($T_{\rm eff}$, $\mu_{1/2} \in [780\text{–}980$ K], $\mu_{1\,\sigma} \sim \pm 20$ K) that bracket previous estimates, depending on model and radius prior choice. In our retrievals where we parameterize the effects of disequilibrium chemistry using a quench pressure, we find large (deep) quench pressure values ($P_{\rm quench}$, $\mu_{1/2} \sim 2.4\text{–}2.8$ bars, $\mu_{1\,\sigma} \sim \pm 0.05$ bars), indicating uniform and out-of-equilibrium abundances of H_2O, CO, and CH_4 in the photosphere. This is in good agreement with Z. Zhang et al. (2023) and K. Franson et al. (2024), although our revised values are slightly lower than theirs, due to our lower-metallicity estimate. The retrievals also indicate that because of the degeneracy with the restrictive radius prior and *P–T* profile, the exact estimation of $P_{\rm quench}$ is influenced by the small-radius problem. Hopefully, higher-resolution measurements with HiRISE (e.g., A. Vigan et al. 2024) or KPIC (e.g., J. W. Xuan et al. 2024a) will be able to probe a wider range of pressures, and their abundance estimates will therefore be less sensitive to these degeneracies. Spectral observations at longer wavelengths with JWST (e.g., GO-5342, PI: Xuan) will help to better constrain the abundances of C- and O-bearing molecules. Given the improvement in the radius determination between `Exo-REM` and other forward models, it is reasonable to expect that changes in the cloud modeling (considering particle size distributions better informed by microphysics) or inhomogeneous clouds in retrievals could help alleviate the small-radius problem and enable better constraints on the planet's fundamental properties.

For now we adopt, from a combination of the median of the range of our forward models and retrievals and inflating the typical uncertainties on the median by a factor of two, the following parameter range estimates for the atmosphere of AF Lep b: $T_{\rm eff} = 800 \pm 50$ K, $\log(g) = 3.7 \pm 0.2$, $R = 1.3 R_{\rm J} \pm 0.15 R_{\rm J}$, [Fe/H] $= 0.75 \pm 0.25$, C/O $= 0.55 \pm .10$, $P_{\rm quench} = 2.6^{+0.2}_{-0.3}$.

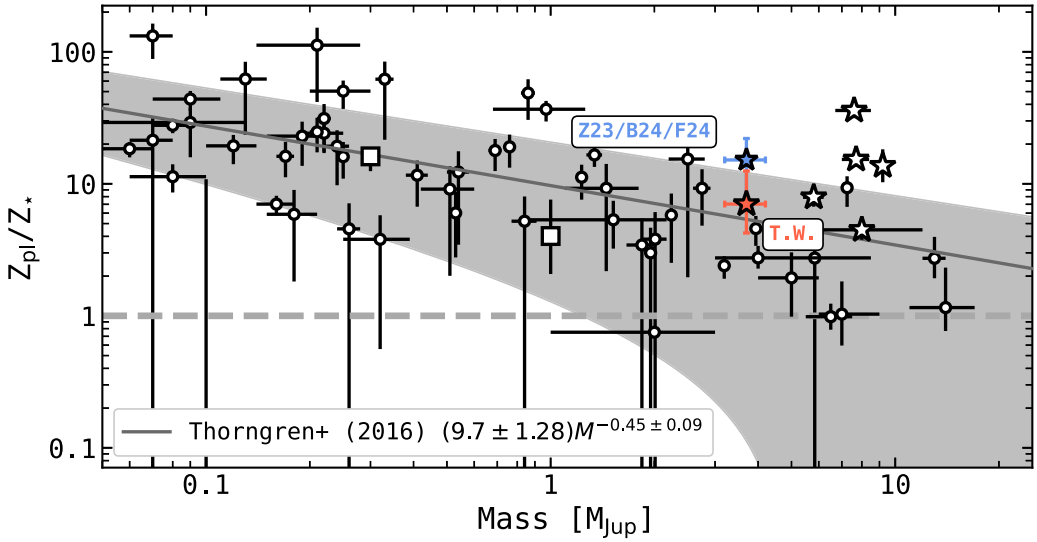

Figure 10. The mass–metallicity relationship for giant exoplanets, adapted from D. P. Thorngren et al. (2016) and E. Nasedkin et al. (2024b) and references therein. AF Lep b from this work is indicated by a red star, while AF Lep b with the mass from M. J. Bonse et al. (2024) and metallicity from Z. Zhang et al. (2023) and K. Franson et al. (2024) is indicated by a blue star. Other planets that have metallicities estimated based partially on GRAVITY spectra and `petitRADTRANS` retrievals, namely β-Pictoris b (GRAVITY Collaboration et al. 2020) and the HR 8799 planets (P. Mollière et al. 2020; E. Nasedkin et al. 2024b), are indicated with black stars. The solar system gas giants, Jupiter and Saturn, are indicated with squares, with bulk abundances from T. Guillot (1999) and D. P. Thorngren et al. (2016). Note that, unlike the other error bars that only include the uncertainty on the planetary abundances, the uncertainties for AF Lep b include the uncertainty on the stellar abundances and the planetary abundances combined.

4.5. Hints at Formation History from an Initial Atmospheric Analysis

Formation via core accretion (or within a disk more generally) could encode a specific atmospheric C/O and metallicity, depending on the location of formation in relation to various snowlines, where gaseous molecules condense into solid icy grains (K. I. Öberg et al. 2011), and the subsequent accretion history of the planet. The actual measurement of these quantities, especially C/O, via atmospheric modeling has proven difficult (see discussion in K. K. W. Hoch et al. 2023), even for benchmark brown dwarf companions with better-constrained fundamental properties (see e.g., M. R. Line et al. 2015; K. K. Wilcomb et al. 2020; E. Calamari et al. 2022; J. Wang et al. 2022; J. W. Xuan et al. 2022; W. O. Balmer et al. 2023; M. J. Rowland et al. 2023; E. Calamari et al. 2024; J. W. Xuan et al. 2024a). Nevertheless, significant progress has been made in the past decade on directly imaged objects (e.g., Q. M. Konopacky et al. 2013; P. Mollière et al. 2020; J. J. Wang et al. 2020; J. J. Wang et al. 2021a; K. K. W. Hoch et al. 2023; J. Wang et al. 2023; E. Nasedkin et al. 2024b). Provided that the measurement can be made accurately enough for the planet, the interpretation of planetary C/O ratios is especially sensitive to planetary formation model assumptions (P. Mollière et al. 2022), as well as to measurements of the baseline host star abundances (H. Reggiani et al. 2022, 2024).

The planet's metallicity ($[\mathrm{M/H}] = 0.75 \pm 0.25$) appears straightforward to interpret in the context of core accretion. Transiting giant exoplanets appear to follow a mass–metallicity relationship (T. Guillot et al. 2006; N. Miller & J. J. Fortney 2011; D. P. Thorngren et al. 2016) consistent with expectations from core accretion (Y. Hasegawa et al. 2018). In order to transform our planetary [M/H] estimates into a ratio of $Z_{\mathrm{planet}}/Z_\star$, we assume that the stellar metallicity follows the β Pic moving group proxy metallicity ($[\mathrm{Fe/H}] = +0.13 \pm 0.10$) derived in H. Reggiani et al. (2024). This estimate agrees with the stellar photospheric metallicity of AF Lep A ($[\mathrm{Fe/H}] = -0.27 \pm 0.31$) derived in Z. Zhang et al. (2023) at 2σ, but we use the proxy metallicity here because the photospheric abundances of rapidly rotating early-type stars are more difficult to estimate than their later-type siblings, and the dispersion of metallicities in open clusters is generally of order 0.03 (V. J. Poovelil et al. 2020; see also the discussion in Section 6 of H. Reggiani et al. 2024). Following D. Thorngren & J. J. Fortney (2019, Equations (2)–(3)) and E. Nasedkin et al. (2024b, Equations (18)–(20)) and propagating the uncertainty on the host star metallicity, we transformed $[\mathrm{M/H}] = 0.75 \pm 0.25$ into $Z_{\mathrm{pl}} = 0.073^{+0.050}_{-0.031}$ assuming that the planet is fully mixed (i.e., has no solid core) and derived $Z_{\mathrm{pl}}/Z_\star = 7.0^{+5.5}_{-2.8}$ (or $Z_{\mathrm{pl}}/Z_\star = 2.8^{+10.4}_{-3.7}$, using the stellar [Fe/H] measurement from Z. Zhang et al. 2023). With the dynamical mass from our orbit fit, we plotted AF Lep b in a mass–metallicity diagram with other exoplanets and directly imaged companions (Figure 10). For massive planets ($\gtrsim 2M_J$) the assumption that they are fully mixed, so that their atmospheric metallicity corresponds to their bulk metallicity, is not unfounded (but see discussion in D. Thorngren & J. J. Fortney 2019). AF Lep b shows excellent agreement with the empirical relation fit to warm transiting Jupiters in D. P. Thorngren et al. (2016).

The adopted range of C/O encompasses the solar value, and the adopted metallicity indicates that the planet is metal-rich. Given these facts, we make a highly simplified, illustrative argument about the formation history of AF Lep b. We used the formation inversion model presented in P. Mollière et al. (2022) assuming the static protoplanetary disk model from K. I. Öberg et al. (2011). This model indicates that the planet likely accreted its solids beyond the CO ice line but sets no constraint on where the gas was accreted. In this case, the planetary core might have formed beyond the CO ice line and migrated inward. It is important not to overinterpret this result given the simplistic disk model, however. In P. Mollière et al. (2022) it was shown that in the case of HR 8799 e, with a similar abundance constraint (moderately enhanced [Fe/H],

solar C/O), including the effect of chemical evolution within the disk model resulted in an entirely different formation interpretation; the planet's current orbit and abundance pattern was consistent with in situ formation. Stronger constraints on the planet's abundances or constraints on isotopologues (e.g., J. W. Xuan et al. 2024a) could motivate more detailed formation inversion modeling. Future work should treat the planet formation inversion modeling with more detailed protoplanetary disk models (for instance, models that vary abundances over time as the gas evaporates, or as large dust grains drift inward) and employ a more careful reading of the ratio of planetary to stellar abundance as the planetary C/O becomes more refined (for instance, H. Reggiani et al. 2024 find that their β Pic abundance proxy HD 181327 has a supersolar $C/O = 0.62 \pm 0.08$, which encompasses our estimates at $1\sigma-3\sigma$, depending on the model).

4.6. Constraints on the Properties of Planets Observed with Only Absolute Astrometry and GRAVITY

As in T. O. Winterhalder et al. (2024), we find that coupling absolute astrometry with relative astrometry from GRAVITY results in well-constrained posterior distributions of orbital elements. An orbit fit to the HGCA and our three epochs of GRAVITY relative astrometry (taken over only 2 months) results in a posterior distribution effectively equivalent to that recorded in Table 3 but with wider uncertainties: semimajor axis constrained to within ± 0.5 au, a 1σ upper limit on the eccentricity of 0.05, and an inclination angle to within 2°. This indicates that Gaia-discovered planets directly observed uniquely with GRAVITY will have well-constrained orbital elements (see also the BD examples in T. O. Winterhalder et al. 2024). Our (dis)equilibrium chemistry, agnostic cloud, gradient *P–T* retrieval with a wide radius prior, fit to only the GRAVITY spectrum, found an unphysically small radius $R = 0.70 R_J \pm 0.05 R_J$, slightly subsolar $C/O = 0.50 \pm 0.05$, and a deep quench pressure $P_{quench} \sim 2.67 \pm 0.06$ bars, consistent within $1\sigma-2\sigma$ with the equivalent retrievals performed on the entire SED. Our free chemistry, agnostic cloud, gradient *P–T* retrieval with a wide radius prior, fit to only the GRAVITY spectrum, yielded constraints on the log mass fraction of $H_2O = -2.86 \pm 0.05$, $CO = -2.99 \pm 0.10$, and $CH_4 = -4.99 \pm 0.08$, that is, constraints on the individual molecular abundances to about 5% statistical uncertainty. We find a recombined $C/O = 0.43 \pm 0.06$ for this retrieval, the lowest C/O in our retrieval analysis, which could indicate some missing oxygen contribution from, for instance, solid grains (but this could be solved by a retrieval with greater cloud model fidelity). The cloud properties are unconstrained by the *K*-band spectrum and result in a largely cloudless atmosphere in both cases, but, interestingly, the free chemistry retrieval resulted in a radius ($R = 1.22^{+0.19}_{-0.14} R_J$) that is consistent within 1σ with the expectations from evolutionary models. This indicates that the parameterization of (dis)equilibrium chemistry is more deterministic of the bulk properties of the atmosphere than the free chemistry parameterization. The cloudy `Exo-REM` forward models fit to only the GRAVITY spectrum resulted in multiple solutions, some of which had physically plausible radii. Regardless of current atmospheric model shortcomings, these are very encouraging results for exoplanet science coupling Gaia and GRAVITY, as future observations should be high enough in quality to facilitate comparative studies leveraging the orbital elements (e.g., Figure 17 in B. P. Bowler et al. 2020) or molecular abundances (provided that the systematic uncertainty in the atmospheric results can be marginalized over when comparing between planets fit using the same model framework).

5. Conclusions

We obtained new spectroscopic *K*-band ($R = 500$, 1.9–2.5 μm) interferometric observations of the directly imaged planet AF Lep b using VLTI/GRAVITY, which achieved ~ 50 μas relative astrometric precision and resulted in the direct detection of methane absorption in the planet's atmosphere. We also re-reduced the SPHERE IFS ($R = 30$, 0.95–1.64 μm) spectrum of the planet from D. Mesa et al. (2023) using the `robust PACO` algorithm.

These observations allowed us to measure the orbit of the planet to high precision. The planet's revised dynamical mass is $M_b = 3.75^{+0.5}_{-0.5} M_J$, making AF Lep b one of the lowest-mass directly imaged planets, and consistent with the $<4 M_J$ population of RV planets orbiting metal-rich host stars (a property associated with core accretion formation; N. C. Santos et al. 2017; K. C. Schlaufman 2018). We determined that the planet's orbit is circular to within an upper limit of $e < 0.02$, 0.07, and 0.13 at 1σ, 2σ, 3σ confidence, respectively, and that the planet's orbital inclination ($i_{orbit} = 57.^\circ5^{+0.^\circ6}_{-0.^\circ7}$) is consistent with being aligned with the host star's rotation axis $i_\star = 54^{\circ+11^\circ}_{-9^\circ}$. A circular, aligned orbit is the expected outcome of formation within a protoplanetary disk, and there appears to be growing population-level evidence that supports the hypothesis that directly imaged planets follow this expected outcome (B. P. Bowler et al. 2020, 2023; A. G. Sepulveda et al. 2024). In light of a nondetection of additional, more widely separated gas giant planets from JWST (K. Franson et al. 2024), we show that, given our orbit constraints, $<1/3$ of accepted orbits are sufficiently eccentric to "stir" the outer debris belt at 46 ± 9 au; the maximum a posteriori orbit is inconsistent with stirring the debris and would necessitate another disk-driven process, or additional smaller planets to explain the debris population.

New *K*-band spectroscopy of the planet facilitated an updated atmospheric analysis that represents a departure from previous studies in a few key ways. Reproducing the forward model analysis in P. Palma-Bifani et al. (2024) and the retrieval analysis in Z. Zhang et al. (2023) and adding the new GRAVITY spectrum results in derived radii that are inconsistent with expectations based on the dynamical mass and evolutionary models (and, in some cases, physically impossible radii); it was necessary to fix the radius a priori to recover physically plausible solutions. Nevertheless, noting the general agreement of our atmospheric abundances regardless of the modeled radii, marginalizing over the radius problem (and over the differences between the forward models and retrievals), we determined an updated range of atmospheric parameters for the planet: $T_{eff} = 800 \pm 50$ K, $\log(g) = 3.7 \pm 0.2$, $R = 1.3 R_J \pm 0.15 R_J$, $[Fe/H] = 0.75 \pm 0.25$, $C/O = 0.55 \pm 0.10$. In the context of the planetary mass–metallicity trend, AF Lep b coincides with the relationship fit to the bulk metallicities of warm transiting Jupiters identified in D. P. Thorngren et al. (2016), a trend that is associated with core accretion formation (Y. Hasegawa et al. 2018). We touch briefly on potential future work connecting the atmospheric abundances of the planet with formation models, but we caution that the major limiting factors here are still systematic uncertainties in our atmospheric models and limiting, simplifying assumptions in the protoplanetary disk models that can be considered in this inversion framework (see discussion in P. Mollière et al. 2022).

This work also demonstrates that future observations of ice line separation planets, detected with Gaia absolute astrometry in DR4 and uniquely directly imaged with VLIT/GRAVITY, can constrain the orbits of these planets and the atmospheric abundance of key molecular species. In the near future, continued astrometric monitoring of this planetary system could reveal higher-order signals, like epicycles induced by inner giant planets (S. Lacour et al. 2021) or particularly massive exomoons, while continuing to refine the planet's eccentricity upper limit to assess the stirring of the debris disk. In the next decade, long baseline optical interferometry will enable a census of the formation histories of young gas giant planets detected with absolute astrometry and will better inform our understanding of where, when, and how gas giant planets form.

Acknowledgments

Many thanks to our night astronomers for these service mode observations, Claudia Paladini, Abigail Frost, Julien Drevon, and Thomas Rivinius, and to the telescope operators Alex Correa, Leonel Rivas, and Rodrigo Palominos. We are infinitely grateful to the Paranal and ESO staff for their support. Thanks also to Tim Pearce for discussion of planet–debris interactions. We thank the anonymous reviewer for their constructive response, which helped us improve this manuscript.

This work is based on observations collected at the European Southern Observatory under ESO programs 112.25GE.001, 112.25GE.002, 112.25GE.003.

Part of this work was carried out by W.O.B. at the Advanced Research Computing at Hopkins (ARCH) core facility (rockfish.jhu.edu), which is supported by the National Science Foundation (NSF) grant No. OAC1920103.

This work used the Dutch national e-infrastructure with the support of the SURF Cooperative using grant No. EINF-1620.

K.F. acknowledges support from the National Science Foundation Graduate Research Fellowship Program under grant No. DGE 2137420. T.S. acknowledges the support from the Netherlands Organisation for Scientific Research (NWO) through grant VI.Veni.202.230.

S.L. acknowledges the support of the French Agence Nationale de la Recherche (ANR), under grant ANR-21-CE31-0017 (project ExoVLTI). Z.Z. is supported by NASA Hubble Fellowship grant HST-HF2-51522.001-A. J.J.W., A. C., and S.B. are supported by NASA XRP grant 80NSSC23K0280.

This research has made use of the VizieR catalog access tool, CDS, Strasbourg, France (doi:10.26093/cds/vizier).

This research has made use of the Jean-Marie Mariotti Center `Aspro` service.

This publication makes use of data products from the Two Micron All Sky Survey, which is a joint project of the University of Massachusetts and the Infrared Processing and Analysis Center/California Institute of Technology, funded by the National Aeronautics and Space Administration and the National Science Foundation.

This work has made use of data from the European Space Agency (ESA) mission Gaia (https://www.cosmos.esa.int/gaia), processed by the Gaia Data Processing and Analysis Consortium (DPAC, https://www.cosmos.esa.int/web/gaia/dpac/consortium). Funding for the DPAC has been provided by national institutions, in particular the institutions participating in the Gaia Multilateral Agreement.

This project has received funding from the European Research Council (ERC) under the European Union's Horizon 2020 research and innovation program (COBREX; grant agreement No. 885593).

SPHERE is an instrument designed and built by a consortium consisting of IPAG (Grenoble, France), MPIA (Heidelberg, Germany), LAM (Marseille, France), LESIA (Paris, France), Laboratoire Lagrange (Nice, France), INAF—Osservatorio di Padova (Italy), Observatoire de Genève (Switzerland), ETH Zürich (Switzerland), NOVA (Netherlands), ONERA (France), and ASTRON (Netherlands) in collaboration with ESO. SPHERE was funded by ESO, with additional contributions from CNRS (France), MPIA (Germany), INAF (Italy), FINES (Switzerland), and NOVA (Netherlands). SPHERE also received funding from the European Commission Sixth and Seventh Framework Programmes as part of the Optical Infrared Coordination Network for Astronomy (OPTICON) under grant No. RII3-Ct-2004-001566 for FP6 (2004-2008), grant No. 226604 for FP7 (2009-2012), and grant No. 312430 for FP7 (2013-2016).

This work has made use of the SPHERE Data Centre, jointly operated by OSUG/IPAG (Grenoble), PYTHEAS/LAM/CeSAM (Marseille), OCA/Lagrange (Nice), Observatoire de Paris/LESIA (Paris), and Observatoire de Lyon (OSUL/CRAL).

W.O.B. acknowledges their cat, Morgoth, for her "encouragement."

Appendix
Additional Posterior Distributions

This appendix includes plots representing the posterior distributions for the forward models we present in this paper. The posterior distribution for our `Exo-REM` atmospheric model fit to all observations using `species` is shown in Figure 11, and the fit where we fix the surface gravity to 3.7 is shown in Figure 12.

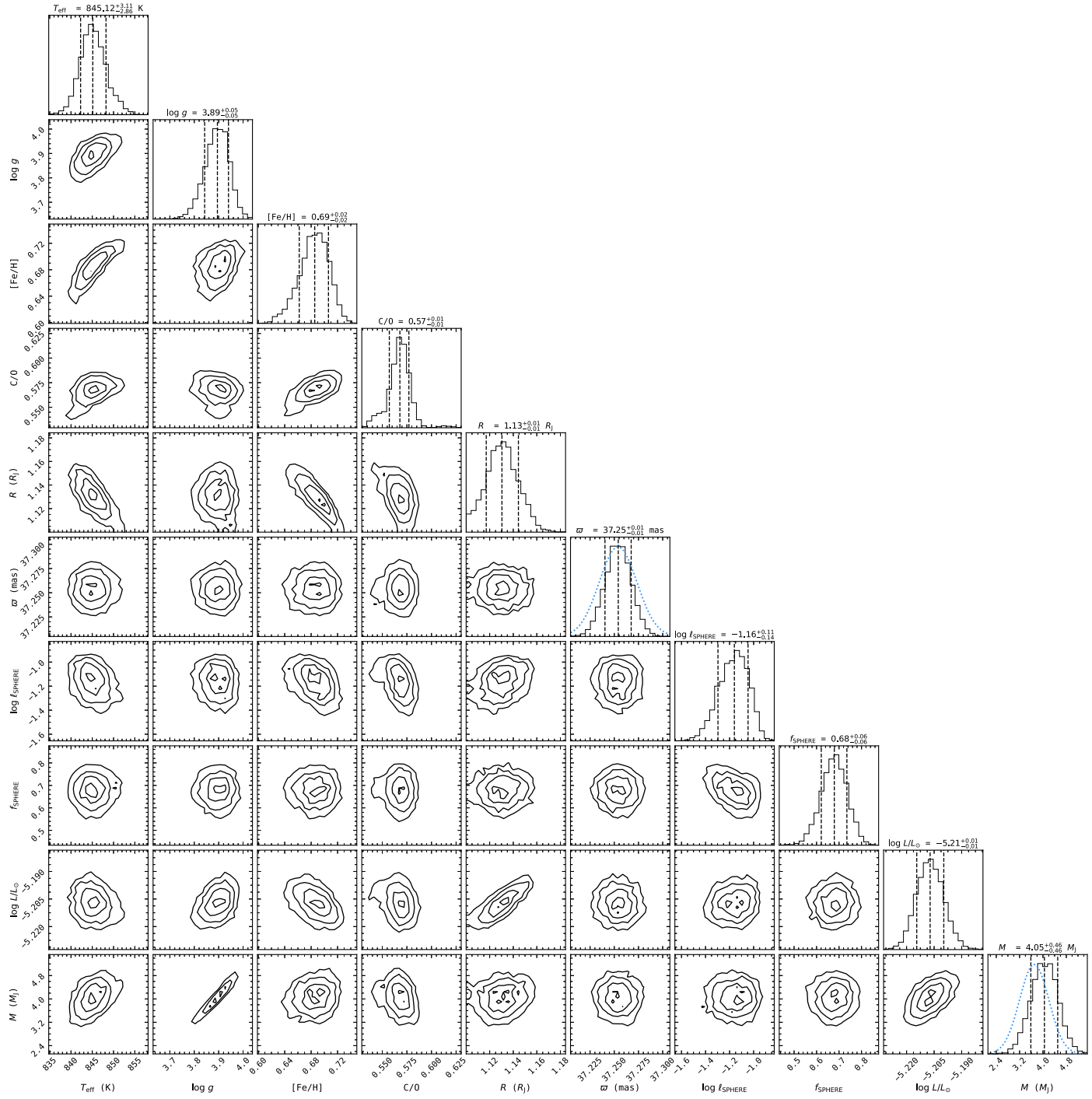

Figure 11. The posterior distribution of atmospheric parameters for the Exo-REM model fit to our observations for the case where log(g) is not fixed to 3.7, but we adopt the dynamical mass as a prior and let log(g), R vary. Light-blue dashed normal distributions plotted over the 1D marginalized posteriors for parallax (ϖ) and planetary mass (M) denote the adopted priors as explained in Section 3.2.

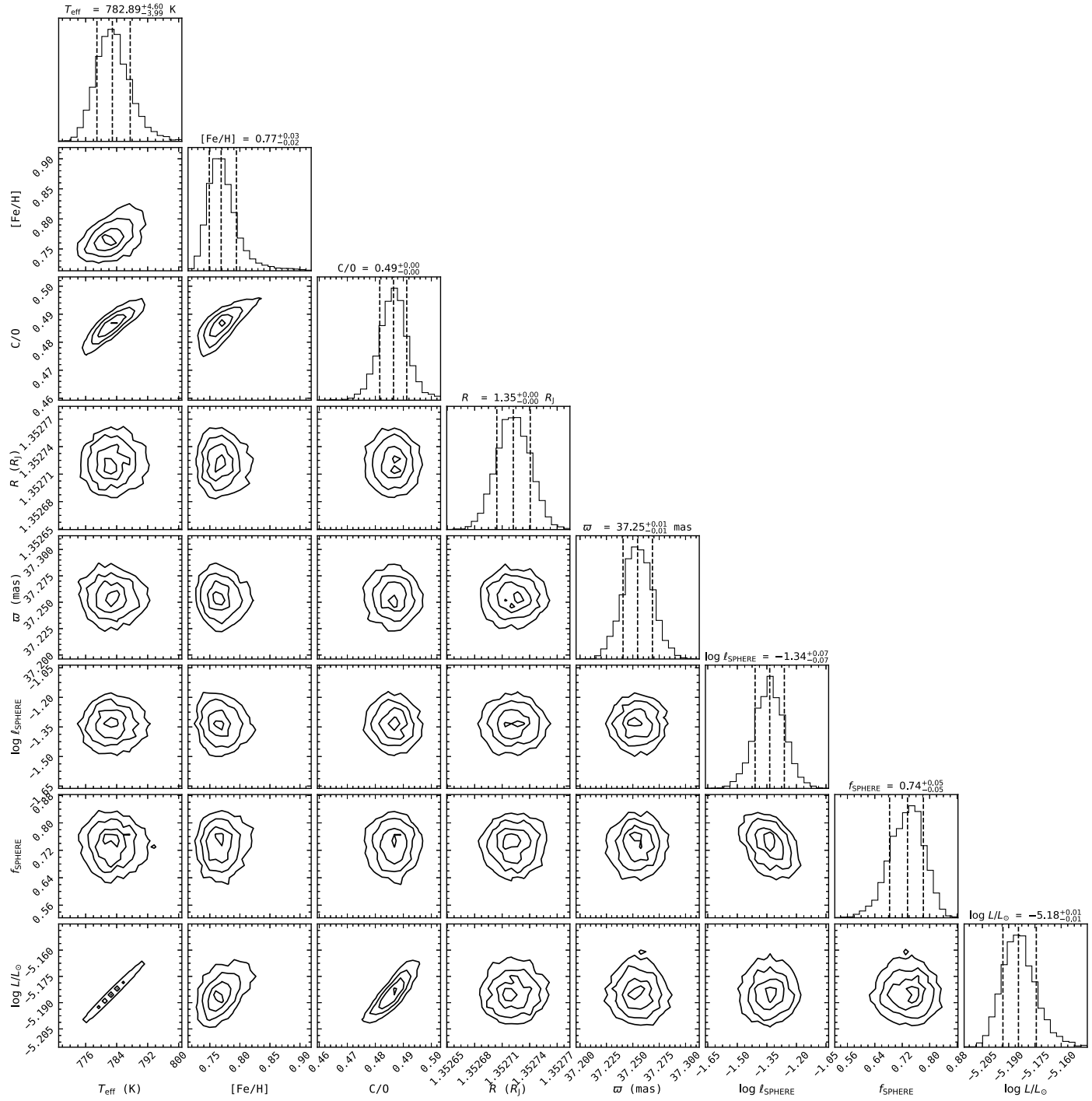

Figure 12. The posterior distribution of atmospheric parameters for the Exo-REM model fit to our observations for the case where log(g) is fixed to 3.7, the mass is fixed to the central value of our dynamical mass, and the resulting radius is 1.35$R_{\rm J}$. Light-blue dashed normal distributions are plotted over the 1D marginalized posteriors for parallax (ϖ) as explained in Section 3.2. Unlike Figure 11, log(g) and mass are not shown, as they were not varied.

ORCID iDs

William O. Balmer https://orcid.org/0000-0001-6396-8439
Kyle Franson https://orcid.org/0000-0003-4557-414X
Antoine Chomez https://orcid.org/0000-0001-5250-9384
Laurent Pueyo https://orcid.org/0000-0003-3818-408X
Tomas Stolker https://orcid.org/0000-0002-5823-3072
Sylvestre Lacour https://orcid.org/0000-0002-6948-0263
Evert Nasedkin https://orcid.org/0000-0002-9792-3121
Markus J. Bonse https://orcid.org/0000-0003-2202-1745
Daniel Thorngren https://orcid.org/0000-0002-5113-8558
Paulina Palma-Bifani https://orcid.org/0000-0002-6217-6867
Paul Mollière https://orcid.org/0000-0003-4096-7067
Jason J. Wang https://orcid.org/0000-0003-0774-6502
Zhoujian Zhang https://orcid.org/0000-0002-3726-4881
Amanda Chavez https://orcid.org/0000-0003-2670-9387
Jens Kammerer https://orcid.org/0000-0003-2769-0438
Sarah Blunt https://orcid.org/0000-0002-3199-2888

Brendan P. Bowler https://orcid.org/0000-0003-2649-2288
Mickael Bonnefoy https://orcid.org/0000-0001-5579-5339
Wolfgang Brandner https://orcid.org/0000-0003-1939-6351
Benjamin Charnay https://orcid.org/0000-0003-0977-6545
Th. Henning https://orcid.org/0000-0002-1493-300X
Nicolas Pourré https://orcid.org/0000-0001-9431-5756
Emily Rickman https://orcid.org/0000-0003-4203-9715
Robert De Rosa https://orcid.org/0000-0002-4918-0247
Arthur Vigan https://orcid.org/0000-0002-5902-7828

References

Ackerman, A. S., & Marley, M. S. 2001, ApJ, 556, 872
Alei, E., Konrad, B. S., Angerhausen, D., et al. 2022, A&A, 665, A106
Allard, F., Homeier, D., & Freytag, B. 2011, in ASP Conf. Ser. 448, 16th Cambridge Workshop on Cool Stars, Stellar Systems, and the Sun, ed. C. Johns-Krull, M. K. Browning, & A. A. West (San Francisco, CA: ASP), 91
Allard, N. F., Spiegelman, F., & Kielkopf, J. F. 2016, A&A, 589, A21
Allard, N. F., Spiegelman, F., Leininger, T., & Mollière, P. 2019, A&A, 628, A120
Azzam, A. A. A., Yurchenko, S. N., Tennyson, J., & Naumenko, O. V. 2016, MNRAS, 460, 4063
Balmer, W. O., Pueyo, L., Lacour, S., et al. 2024, AJ, 167, 64
Balmer, W. O., Pueyo, L., Stolker, T., et al. 2023, ApJ, 956, 99
Barber, R. J., Strange, J. K., Hill, C., et al. 2014, MNRAS, 437, 1828
Barman, T. S., Macintosh, B., Konopacky, Q. M., & Marois, C. 2011a, ApJ, 733, 65
Barman, T. S., Macintosh, B., Konopacky, Q. M., & Marois, C. 2011b, ApJL, 735, L39
Barton, E. J., Chiu, C., Golpayegani, S., et al. 2014, MNRAS, 442, 1821
Barton, E. J., Yurchenko, S. N., & Tennyson, J. 2013, MNRAS, 434, 1469
Bate, M. R. 2009, MNRAS, 392, 590
Bate, M. R. 2012, MNRAS, 419, 3115
Baudino, J. L., Bézard, B., Boccaletti, A., et al. 2015, A&A, 582, A83
Bell, C. P. M., Mamajek, E. E., & Naylor, T. 2015, MNRAS, 454, 593
Biller, B. A., Liu, M. C., Wahhaj, Z., et al. 2013, ApJ, 777, 160
Bitsch, B., Trifonov, T., & Izidoro, A. 2020, A&A, 643, A66
Blunt, S., Balmer, W. O., Wang, J. J., et al. 2023, AJ, 166, 257
Blunt, S., Nielsen, E. L., De Rosa, R. J., et al. 2017, AJ, 153, 229
Blunt, S., Wang, J. J., Angelo, I., et al. 2020, AJ, 159, 89
Bonavita, M., Fontanive, C., Gratton, R., et al. 2022, MNRAS, 513, 5588
Bonse, M. J., Gebhard, T. D., Dannert, F. A., et al. 2024, arXiv:2406.01809
Borysow, A., Frommhold, L., & Moraldi, M. 1989, ApJ, 336, 495
Borysow, A., Jørgensen, U. G., & Fu, Y. 2001, JQSRT, 68, 235
Borysow, J., Frommhold, L., & Birnbaum, G. 1988, ApJ, 326, 509
Boss, A. P. 1997, Sci, 276, 1836
Bowler, B. P., Blunt, S. C., & Nielsen, E. L. 2020, AJ, 159, 63
Bowler, B. P., Liu, M. C., Dupuy, T. J., & Cushing, M. C. 2010, ApJ, 723, 850
Bowler, B. P., Tran, Q. H., Zhang, Z., et al. 2023, AJ, 165, 164
Boyd, D. F. A., & Whitworth, A. P. 2005, A&A, 430, 1059
Brandt, T. D. 2018, ApJS, 239, 31
Brandt, T. D. 2021, ApJS, 254, 42
Buchner, J., Georgakakis, A., Nandra, K., et al. 2014, A&A, 564, A125
Burningham, B., Faherty, J. K., Gonzales, E. C., et al. 2021, MNRAS, 506, 1944
Burningham, B., Marley, M. S., Line, M. R., et al. 2017, MNRAS, 470, 1177
Burrows, A., Hubbard, W. B., Lunine, J. I., & Liebert, J. 2001, RvMP, 73, 719
Butler, R. P., Vogt, S. S., Laughlin, G., et al. 2017, AJ, 153, 208
Calamari, E., Faherty, J. K., Burningham, B., et al. 2022, ApJ, 940, 164
Calamari, E., Faherty, J. K., Visscher, C., et al. 2024, ApJ, 963, 67
Carnall, A. C. 2017, arXiv:1705.05165
Chabrier, G. 2003, PASP, 115, 763
Chabrier, G., Baraffe, I., Phillips, M., & Debras, F. 2023, A&A, 671, A119
Chabrier, G., & Debras, F. 2021, ApJ, 917, 4
Chabrier, G., Mazevet, S., & Soubiran, F. 2019, ApJ, 872, 51
Chabrier, G., & Potekhin, A. Y. 1998, PhRvE, 58, 4941
Chan, Y. M., & Dalgarno, A. 1965, PPS, 85, 227
Charnay, B., Bézard, B., Baudino, J. L., et al. 2018, ApJ, 854, 172
Chilcote, J., Tobin, T., Currie, T., et al. 2021, AJ, 162, 251
Childs, A. C., Quintana, E., Barclay, T., & Steffen, J. H. 2019, MNRAS, 485, 541
Chomez, A., Lagrange, A. M., Delorme, P., et al. 2023, A&A, 675, A205
Chubb, K. L., Rocchetto, M., Yurchenko, S. N., et al. 2021, A&A, 646, A21
Coles, P. A., Yurchenko, S. N., & Tennyson, J. 2019, MNRAS, 490, 4638
Currie, T., Biller, B., Lagrange, A., et al. 2023, in ASP Conf. Ser. 534, Protostars and Planets VII, ed. S. Inutsuka et al. (San Francisco, CA: ASP), 799
Currie, T., Brandt, T. D., Kuzuhara, M., et al. 2020, ApJL, 904, L25
Cutri, R. M., Skrutskie, M. F., van Dyk, S., et al. 2003, yCat, II/246
Czekala, I., Andrews, S. M., Mandel, K. S., Hogg, D. W., & Green, G. M. 2015, ApJ, 812, 128
Dalgarno, A., & Williams, D. A. 1962, ApJ, 136, 690
De Rosa, R. J., Nielsen, E. L., Wahhaj, Z., et al. 2023, A&A, 672, A94
Delorme, P., Meunier, N., Albert, D., et al. 2017, in SF2A-2017: Proc. Annual meeting of the French Society of Astronomy and Astrophysics, ed. C. Reylé et al. (Paris: French Society of Astronomy and Astrophysics), 347
Do Ó, C. R., O'Neil, K. K., Konopacky, Q. M., et al. 2023, AJ, 166, 48
Emsenhuber, A., Mordasini, C., Burn, R., et al. 2021a, A&A, 656, A69
Emsenhuber, A., Mordasini, C., Burn, R., et al. 2021b, A&A, 656, A70
Faherty, J. K., Riedel, A. R., Cruz, K. L., et al. 2016, ApJS, 225, 10
Fernandes, R. B., Mulders, G. D., Pascucci, I., Mordasini, C., & Emsenhuber, A. 2019, ApJ, 874, 81
Feroz, F., & Hobson, M. P. 2008, MNRAS, 384, 449
Feroz, F., Hobson, M. P., & Bridges, M. 2009, MNRAS, 398, 1601
Fischer, D. A., & Valenti, J. 2005, ApJ, 622, 1102
Flasseur, O., Denis, L., Thiébaut, É., & Langlois, M. 2018, A&A, 618, A138
Flasseur, O., Denis, L., Thiébaut, É., & Langlois, M. 2020a, A&A, 634, A2
Flasseur, O., Denis, L., Thiébaut, É., & Langlois, M. 2020b, A&A, 637, A9
Foreman-Mackey, D., Hogg, D. W., Lang, D., & Goodman, J. 2013, PASP, 125, 306
Forgan, D. H., Hall, C., Meru, F., & Rice, W. K. M. 2018, MNRAS, 474, 5036
Franson, K., Balmer, W. O., Bowler, B. P., et al. 2024, ApJL, 974, L11
Franson, K., Bowler, B. P., Bonavita, M., et al. 2023a, AJ, 165, 39
Franson, K., Bowler, B. P., Zhou, Y., et al. 2023b, ApJL, 950, L19
Fulton, B. J., Rosenthal, L. J., Hirsch, L. A., et al. 2021, ApJS, 255, 14
Gaia Collaboration, Vallenari, A., Brown, A. G. A., et al. 2023, A&A, 674, A1
Gao, P., Wakeford, H. R., Moran, S. E., & Parmentier, V. 2021, JGRE, 126, e06655
Gonzales, E. C., Burningham, B., Faherty, J. K., et al. 2020, ApJ, 905, 46
Gonzales, E. C., Burningham, B., Faherty, J. K., et al. 2022, ApJ, 938, 56
Gonzalez, G. 1997, MNRAS, 285, 403
Grandjean, A., Lagrange, A. M., Beust, H., et al. 2019, A&A, 627, L9
Gratton, R., Bonavita, M., Mesa, D., et al. 2024, A&A, 684, A69
GRAVITY Collaboration, Abuter, R., Accardo, M., et al. 2017, A&A, 602, A94
GRAVITY Collaboration, Lacour, S., Nowak, M., et al. 2019, A&A, 623, L11
GRAVITY Collaboration, Nowak, M., Lacour, S., et al. 2020, A&A, 633, A110
Greco, J. P., & Brandt, T. D. 2016, ApJ, 833, 134
Guillot, T. 1999, P&SS, 47, 1183
Guillot, T. 2005, AREPS, 33, 493
Guillot, T., Santos, N. C., Pont, F., et al. 2006, A&A, 453, L21
Hasegawa, Y., Bryden, G., Ikoma, M., Vasisht, G., & Swain, M. 2018, ApJ, 865, 32
Helling, C. 2019, AREPS, 47, 583
Helling, C., Ackerman, A., Allard, F., et al. 2008, MNRAS, 391, 1854
Henning, T., & Stognienko, R. 1996, A&A, 311, 291
Hinkley, S., Lacour, S., Marleau, G. D., et al. 2023, A&A, 671, L5
Hoch, K. K. W., Konopacky, Q. M., Theissen, C. A., et al. 2023, AJ, 166, 85
Høg, E., Fabricius, C., Makarov, V. V., et al. 2000, A&A, 355, L27
Hood, C. E., Fortney, J. J., Line, M. R., & Faherty, J. K. 2023, ApJ, 953, 170
Horner, J., Kane, S. R., Marshall, J. P., et al. 2020a, PASP, 132, 102001
Horner, J., Vervoort, P., Kane, S. R., et al. 2020b, AJ, 159, 10
Hubbard, W. B., Burrows, A., & Lunine, J. I. 2002, ARA&A, 40, 103
Jaeger, C., Molster, F. J., Dorschner, J., et al. 1998, A&A, 339, 904
Kammerer, J., Lacour, S., Stolker, T., et al. 2021, A&A, 652, A57
Karalidi, T., Marley, M., Fortney, J. J., et al. 2021, ApJ, 923, 269
Kervella, P., Arenou, F., Mignard, F., & Thévenin, F. 2019, A&A, 623, A72
Kervella, P., Arenou, F., & Thévenin, F. 2022, A&A, 657, A7
Kitzmann, D., Heng, K., Oreshenko, M., et al. 2020, ApJ, 890, 174
Konopacky, Q. M., Barman, T. S., Macintosh, B. A., & Marois, C. 2013, Sci, 339, 1398
Kratter, K. M., Murray-Clay, R. A., & Youdin, A. N. 2010, ApJ, 710, 1375
Krivov, A. V., & Booth, M. 2018, MNRAS, 479, 3300
Lacour, S., Dembet, R., Abuter, R., et al. 2019, A&A, 624, A99
Lacour, S., Wang, J. J., Nowak, M., et al. 2020, Proc. SPIE, 11446, 114460O
Lacour, S., Wang, J. J., Rodet, L., et al. 2021, A&A, 654, L2
Lacy, B., & Burrows, A. 2023, ApJ, 950, 8
Lagrange, A. M., Philipot, F., Rubini, P., et al. 2023, A&A, 677, A71

Lagrange, A. M., Rubini, P., Nowak, M., et al. 2020, A&A, 642, A18
Lapeyrere, V., Kervella, P., Lacour, S., et al. 2014, Proc. SPIE, 9146, 91462D
Launhardt, R., Henning, T., Quirrenbach, A., et al. 2020, A&A, 635, A162
Lee, J., & Song, I. 2024, ApJ, 967, 113
Levison, H. F., & Agnor, C. 2003, AJ, 125, 2692
Li, Y., Brandt, T. D., Brandt, G. M., et al. 2023, MNRAS, 522, 5622
Line, M. R., Teske, J., Burningham, B., Fortney, J. J., & Marley, M. S. 2015, ApJ, 807, 183
Liu, M. C., Dupuy, T. J., & Allers, K. N. 2016, ApJ, 833, 96
Lucy, L. B., & Sweeney, M. A. 1971, AJ, 76, 544
Lueber, A., Kitzmann, D., Bowler, B. P., Burgasser, A. J., & Heng, K. 2022, ApJ, 930, 136
Luna, J. L., & Morley, C. V. 2021, ApJ, 920, 146
Madhusudhan, N. 2018, in Handbook of Exoplanets, ed. H. J. Deeg & J. A. Belmonte, 104
Marcus, P. S. 1993, ARA&A, 31, 523
Marleau, G.-D., Coleman, G. A. L., Leleu, A., & Mordasini, C. 2019, A&A, 624, A20
Marley, M. S., & Robinson, T. D. 2015, ARA&A, 53, 279
Marley, M. S., Saumon, D., Cushing, M., et al. 2012, ApJ, 754, 135
Marley, M. S., Saumon, D., Visscher, C., et al. 2021, ApJ, 920, 85
Marois, C., Macintosh, B., Barman, T., et al. 2008, Sci, 322, 1348
Marois, C., Zuckerman, B., Konopacky, Q. M., Macintosh, B., & Barman, T. 2010, Natur, 468, 1080
McKemmish, L. K., Masseron, T., Hoeijmakers, H. J., et al. 2019, MNRAS, 488, 2836
McKemmish, L. K., Yurchenko, S. N., & Tennyson, J. 2016, MNRAS, 463, 771
Mesa, D., Gratton, R., Kervella, P., et al. 2023, A&A, 672, A93
Mesa, D., Gratton, R., Zurlo, A., et al. 2015, A&A, 576, A121
Miller, N., & Fortney, J. J. 2011, ApJL, 736, L29
Min, M., Hovenier, J. W., & de Koter, A. 2005, A&A, 432, 909
Mollière, P., Molyarova, T., Bitsch, B., et al. 2022, ApJ, 934, 74
Mollière, P., Stolker, T., Lacour, S., et al. 2020, A&A, 640, A131
Mollière, P., van Boekel, R., Bouwman, J., et al. 2017, A&A, 600, A10
Mollière, P., Wardenier, J. P., van Boekel, R., et al. 2019, A&A, 627, A67
Mordasini, C., Alibert, Y., & Benz, W. 2009, A&A, 501, 1139
Mordasini, C., Alibert, Y., Benz, W., Klahr, H., & Henning, T. 2012, A&A, 541, A97
Morrison, D. 1982, ARA&A, 20, 469
Mukherjee, S., Fortney, J. J., Batalha, N. E., et al. 2022, ApJ, 938, 107
Mukherjee, S., Fortney, J. J., Morley, C. V., et al. 2024, ApJ, 963, 73
Mustill, A. J., & Wyatt, M. C. 2009, MNRAS, 399, 1403
Nagpal, V., Blunt, S., Bowler, B. P., et al. 2023, AJ, 165, 32
Nasedkin, E., Mollière, P., & Blain, D. 2024a, JOSS, 9, 5875
Nasedkin, E., Mollière, P., Lacour, S., et al. 2024b, A&A, 687, A298
Nasedkin, E., Mollière, P., Wang, J., et al. 2023, A&A, 678, A41
Nielsen, E. L., De Rosa, R. J., Macintosh, B., et al. 2019, AJ, 158, 13
Nowak, M., Lacour, S., Abuter, R., et al. 2024a, A&A, 684, A184
Nowak, M., Lacour, S., Abuter, R., et al. 2024b, A&A, 687, A248
Nowak, M., Lacour, S., Lagrange, A. M., et al. 2020, A&A, 642, L2
Öberg, K. I., Murray-Clay, R., & Bergin, E. A. 2011, ApJL, 743, L16
Padoan, P., & Nordlund, Å. 2004, ApJ, 617, 559
Palma-Bifani, P., Chauvin, G., Borja, D., et al. 2024, A&A, 683, A214
Pavlov, A., Feldt, M., & Henning, T. 2008, in ASP Conf. Ser. 394, Astronomical Data Analysis Software and Systems XVII, ed. R. W. Argyle, P. S. Bunclark, & J. R. Lewis (San Francisco, CA: ASP), 581
Pearce, T. D., Launhardt, R., Ostermann, R., et al. 2022, A&A, 659, A135
Perryman, M., Hartman, J., Bakos, G. Á., & Lindegren, L. 2014, ApJ, 797, 14
Phillips, M. W., Tremblin, P., Baraffe, I., et al. 2020, A&A, 637, A38
Polyansky, O. L., Kyuberis, A. A., Zobov, N. F., et al. 2018, MNRAS, 480, 2597
Poovelil, V. J., Zasowski, G., Hasselquist, S., et al. 2020, ApJ, 903, 55
Pourré, N., Winterhalder, T. O., Le Bouquin, J. B., et al. 2024, A&A, 686, A258
Raymond, S. N. 2008, in IAU Symp. 249, Exoplanets: Detection, Formation and Dynamics, ed. Y.-S. Sun, S. Ferraz-Mello, & J.-L. Zhou (Cambridge: Cambridge Univ. Press), 233
Raymond, S. N., Armitage, P. J., Moro-Martín, A., et al. 2012, A&A, 541, A11
Raymond, S. N., & Izidoro, A. 2017, Icar, 297, 134
Raymond, S. N., Kokubo, E., Morbidelli, A., Morishima, R., & Walsh, K. J. 2014, in Protostars and Planets VI, ed. H. Beuther et al. (Tucson, AZ: Univ. Arizona Press), 595
Raymond, S. N., & Morbidelli, A. 2022, in Astrophysics and Space Science Library, Demographics of Exoplanetary Systems, Lecture Notes of the 3rd Advanced School on Exoplanetary Science, ed. K. Biazzo et al., Vol. 466 (Cham: Springer), 3
Reggiani, H., Galarza, J. Y., Schlaufman, K. C., et al. 2024, AJ, 167, 45
Reggiani, H., Schlaufman, K. C., Healy, B. F., Lothringer, J. D., & Sing, D. K. 2022, AJ, 163, 159
Richard, C., Gordon, I. E., Rothman, L. S., et al. 2012, JQSRT, 113, 1276
Rosenthal, L. J., Howard, A. W., Knutson, H. A., & Fulton, B. J. 2024, ApJS, 270, 1
Rosenthal, L. J., Knutson, H. A., Chachan, Y., et al. 2022, ApJS, 262, 1
Rothman, L. S., Gordon, I. E., Barber, R. J., et al. 2010, JQSRT, 111, 2139
Rowland, M. J., Morley, C. V., & Line, M. R. 2023, ApJ, 947, 6
Samra, D., Helling, C., & Birnstiel, T. 2022, A&A, 663, A47
Sanghi, A., Liu, M. C., Best, W. M., et al. 2023, ApJ, 959, 63
Santos, N. C., Adibekyan, V., Figueira, P., et al. 2017, A&A, 603, A30
Santos, N. C., Israelian, G., & Mayor, M. 2004, A&A, 415, 1153
Saumon, D., & Marley, M. S. 2008, ApJ, 689, 1327
Schlaufman, K. C. 2018, ApJ, 853, 37
Scott, A., & Duley, W. W. 1996, ApJS, 105, 401
Sepulveda, A. G., Huber, D., Bedding, T. R., et al. 2024, AJ, 168, 13
Skemer, A. J., Close, L. M., Szűcs, L., et al. 2011, ApJ, 732, 107
Sotiriadis, S., Libert, A.-S., & Raymond, S. N. 2018, A&A, 613, A59
Sousa-Silva, C., Al-Refaie, A. F., Tennyson, J., & Yurchenko, S. N. 2015, MNRAS, 446, 2337
Stolker, T., Quanz, S. P., Todorov, K. O., et al. 2020, A&A, 635, A182
Stone, J. M., Skemer, A. J., Hinz, P. M., et al. 2018, AJ, 156, 286
Thorngren, D., & Fortney, J. J. 2019, ApJL, 874, L31
Thorngren, D. P., Fortney, J. J., Murray-Clay, R. A., & Lopez, E. D. 2016, ApJ, 831, 64
Toon, O. B., & Ackerman, T. P. 1981, ApOpt, 20, 3657
Tremblin, P., Amundsen, D. S., Mourier, P., et al. 2015, ApJL, 804, L17
Vahidinia, S., Moran, S. E., Marley, M. S., & Cuzzi, J. N. 2024, PASP, 136, 084404
Vigan, A., El Morsy, M., Lopez, M., et al. 2024, A&A, 682, A16
Vigan, A., Fontanive, C., Meyer, M., et al. 2021, A&A, 651, A72
Vos, J. M., Burningham, B., Faherty, J. K., et al. 2023, ApJ, 944, 138
Vos, J. M., Faherty, J. K., Gagné, J., et al. 2022, ApJ, 924, 68
Vousden, W. D., Farr, W. M., & Mandel, I. 2016, MNRAS, 455, 1919
Wahhaj, Z., Milli, J., Romero, C., et al. 2021, A&A, 648, A26
Wang, J., Kolecki, J. R., Ruffio, J.-B., et al. 2022, AJ, 163, 189
Wang, J., Wang, J. J., Ruffio, J.-B., et al. 2023, AJ, 165, 4
Wang, J. J., Ginzburg, S., Ren, B., et al. 2020, AJ, 159, 263
Wang, J. J., Ruffio, J.-B., Morris, E., et al. 2021a, AJ, 162, 148
Wang, J. J., Vigan, A., Lacour, S., et al. 2021b, AJ, 161, 148
Wende, S., Reiners, A., Seifahrt, A., & Bernath, P. F. 2010, A&A, 523, A58
Wilcomb, K. K., Konopacky, Q. M., Barman, T. S., et al. 2020, AJ, 160, 207
Winterhalder, T. O., Lacour, S., Mérand, A., et al. 2024, A&A, 688, A44
Wittenmyer, R. A., Wang, S., Horner, J., et al. 2020, MNRAS, 492, 377
Xuan, J. W., Hsu, C.-C., Finnerty, L., et al. 2024a, ApJ, 970, 71
Xuan, J. W., Wang, J., Finnerty, L., et al. 2024b, ApJ, 962, 10
Xuan, J. W., Wang, J., Ruffio, J.-B., et al. 2022, ApJ, 937, 54
Yurchenko, S. N., Amundsen, D. S., Tennyson, J., & Waldmann, I. P. 2017, A&A, 605, A95
Yurchenko, S. N., Mellor, T. M., Freedman, R. S., & Tennyson, J. 2020, MNRAS, 496, 5282
Zakamska, N. L., Pan, M., & Ford, E. B. 2011, MNRAS, 410, 1895
Zalesky, J. A., Line, M. R., Schneider, A. C., & Patience, J. 2019, ApJ, 877, 24
Zhang, X., West, R. A., Banfield, D., & Yung, Y. L. 2013, Icar, 226, 159
Zhang, Z. 2024, RNAAS, 8, 114
Zhang, Z., Liu, M. C., Marley, M. S., Line, M. R., & Best, W. M. J. 2021a, ApJ, 916, 53
Zhang, Z., Liu, M. C., Marley, M. S., Line, M. R., & Best, W. M. J. 2021b, ApJ, 921, 95
Zhang, Z., Mollière, P., Hawkins, K., et al. 2023, AJ, 166, 198